Functional geometry of auditory cortical resting state networks derived from intracranial electrophysiology

Matthew I. Banks[1,2*], Bryan M. Krause[1], D. Graham Berger[1], Declan I. Campbell[1], Aaron D. Boes[3], Joel E. Bruss[3], Christopher K. Kovach[4], Hiroto Kawasaki[4], Mitchell Steinschneider[5,6], Kirill V. Nourski[4,7]

[1]Department of Anesthesiology, University of Wisconsin, Madison, WI, USA
[2]Department of Neuroscience, University of Wisconsin, Madison, WI, USA
[3]Department of Neurology, The University of Iowa, Iowa City, IA 52242, USA
[4]Department of Neurosurgery, The University of Iowa, Iowa City, IA 52242, USA
[5]Department of Neurology, Albert Einstein College of Medicine, New York, NY 10461, USA
[6]Department of Neuroscience, Albert Einstein College of Medicine, New York, NY 10461, USA
[7]Iowa Neuroscience Institute, The University of Iowa, Iowa City, IA 52242, USA

***Corresponding author:**

Matthew I. Banks, Ph.D.
Professor
Department of Anesthesiology
University of Wisconsin
1300 University Avenue, Room 4605
Madison, WI 53706
Tel.: (608)261-1143
E-mail: mibanks@wisc.edu

Keywords:

Functional connectivity, hierarchy, fMRI, diffusion map embedding, electrocorticography, iEEG, ECoG

Acknowledgements

This work was supported by the National Institutes of Health (grant numbers R01-DC04290, R01-GM109086). We are grateful to Jess Banks, Alex Billig, Haiming Chen, Matthew Howard, and Ariane Rhone for help with data collection, analysis, and comments on the manuscript.

Abstract

Critical details remain unresolved about the organization of the human auditory cortical hierarchy and its relationship to higher order brain networks. We investigated this organization using diffusion map embedding (DME) applied to resting state intracranial electroencephalography (iEEG) obtained in neurosurgical patients. DME was applied to functional connectivity measured between regions of interest (ROIs). ROIs exhibited a hierarchical organization, symmetric between the two hemispheres and robust to the choice of iEEG frequency band, connectivity metric, and imaging modality. Tight clusters of canonical auditory and prefrontal ROIs were maximally segregated in embedding space. Clusters consistent with ventral and dorsal auditory processing streams were paralleled by a cluster suggestive of a third stream linking auditory and limbic structures. Portions of anterior temporal cortex were characterized as global hubs. This approach lays the foundation for elucidating network changes underlying transitions of arousal state, disorders of consciousness, and during active speech and language processing.

Introduction

Decades of investigation in nonhuman primates and humans have elucidated the organization of the visual cortical hierarchy in considerable detail (e.g.,[1, 2]). By contrast, parallel efforts to understand the organization of the human auditory cortical hierarchy have left unresolved several key questions. Their resolution would advance our understanding of speech and language processing and of the role of audition in cognitive functions of the brain. Although classical descriptions assigned speech comprehension and speech production to specific regions of left temporo-parietal and left inferior frontal cortex, respectively[3], evidence over the last several decades places these functions within a broader, bilateral hierarchy[4]. However, the position of several cortical regions within this hierarchy and their functional relationships remain to be elucidated. The rostral superior temporal areas, including the anterior portion of the superior temporal gyrus and the planum polare, are functionally distinct from immediately adjacent canonical auditory cortex on Heschl's gyrus[5, 6]. Conversely, the posterior portion of the insula has properties similar to those of core auditory cortex in the posteromedial portion of Heschl's gyrus, yet is not considered part of canonical auditory cortex[7]. Additionally, the upper and lower bank of the superior temporal sulcus have distinct roles in speech and language processing[8, 9], yet their distinct functional relationships with the rest of the auditory hierarchy remain to be demonstrated.

Models of functional relationships within auditory processing hierarchy have been proposed by analogy with models of the visual cortical hierarchy[10, 11]. In these models, regions are organized along two processing streams[12-14]. The specific brain regions involved and their functional relationships within each stream remain subjects of vigorous debate[15-17]. This lack of consensus is particularly surprising given the large number of functional and structural MRI studies that have explored the organization of auditory networks, including those subserving speech processing (reviewed in[18, 19]. Furthermore, bidirectional message passing between canonical auditory and limbic areas[20] may be construed as evidence for a third "limbic" auditory processing stream. Hippocampus, amygdala and the anterior portion of the insula are key structures in both auditory working memory and processing of emotional aspects of auditory information[21-24]. These functions are complementary to those of the dorsal and ventral streams, yet the concept of the limbic auditory processing stream has not been emphasized in the literature.

While hemispheric lateralization of speech and language processing is a widely accepted organizational feature, the degree to which it shapes the auditory hierarchy is unknown[16, 25]. For example, planum temporale, lateral superior temporal gyrus, superior temporal sulcus, and inferior frontal gyrus have been characterized as having distinct functional asymmetries in speech processing[12, 25-28]. Whether these asymmetries are reflected in hemisphere-specific connectivity profiles is unclear.

This study addressed these questions by examining the organization of the human auditory processing hierarchy within the broader context of human cortical networks. The analysis was

based on intracranial electroencephalographic (iEEG) recordings in a large number of neurosurgical patients. Although previous studies have investigated connectivity of specific subregions within the auditory cortical hierarchy using structural and functional MRI[8, 29, 30], iEEG recordings offer superior spatio-temporal resolution and do not suffer from methodological problems that affect fMRI in key regions such as the anterior temporal lobe[31, 32]. Functional connectivity was calculated at the level of regions of interest (ROIs) based on an auditory-centric cortical parcellation scheme. Diffusion map embedding (DME;[33, 34] was used to investigate the intrinsic or functional geometry of these ROIs by mapping them into a Euclidean space where distance reflects the functional relationships between the ROIs. DME allows for dimensionality reduction and clustering of data based on these relationships: ROIs that are strongly related are clustered together and are distinct from other clusters of strongly related ROIs. DME has been previously applied to fMRI data to demonstrate the hierarchical structure of canonical resting state (RS) networks[35]. Here, we applied DME to iEEG data for the first time to focus on the functional organization of human auditory cortical networks.

Results

Intracranial electrodes densely sampled cortical structures involved in auditory processing in the temporal and parietal lobes, as well a large number of sites within prefrontal, sensorimotor, and other ROIs throughout the brain (Fig. 1; Supplementary Tables 1 and 2). DME was applied to pairwise functional connectivity computed between recording sites in each subject (Fig. 2). On average, each subject contributed 141±54 recording sites, representing 28±7.9 ROIs (mean ± standard deviation). Electrode coverage in an exemplary subject is shown in Figure 2a. The matrix of functional connectivity was normalized and thresholded by row to yield a transition probability matrix **P** (Fig. 2b). This matrix has an apparent community structure, as evidenced by block structure along the horizontal and vertical dimensions. DME reveals the functional geometry of the sampled cortical sites by mapping the data of **P** into a multidimensional embedding space in which distance between nodes represents similarity in their functional connectivity to the rest of the network (Fig. 2c; three different 2D views, see Supplementary Fig. 1 for three additional views). At the single-subject level, this approach exhibited superior signal-to noise characteristics compared to direct analysis of functional connectivity in 40 out of 46 subjects (Supplementary Fig. 2).

Recording sites that belonged to specific ROIs distributed to specific locations in embedding space. For example, tight clusters of canonical auditory cortical sites and of PFC sites were maximally segregated along dimension 1. Sites belonging to other ROIs (e.g., MTGP) had a more distributed representation, consistent with the functional heterogeneity of these ROIs.

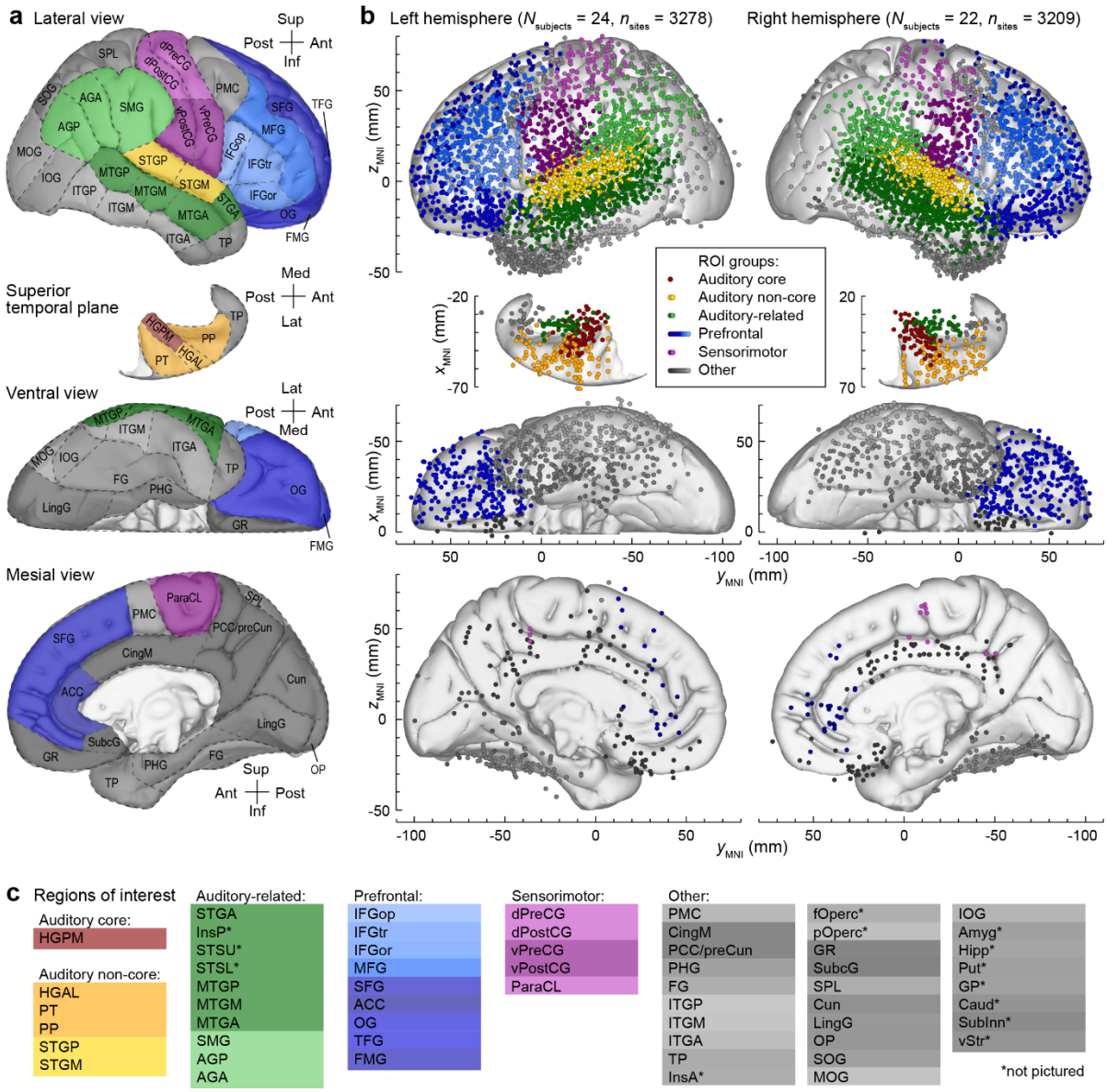
a Lateral view
Sup
Post
Ant
Inf
SPL
dPreCG
dPostCG
PMC
SOG
AGA
SMG
SFG
TFG
AGP
vPostCG
vPreCG
MFG
MOG
IFGop
IFGtr
STGP
IOG
MTGP
STGM
ITGP
MTGM
IFGor
ITGM
STGA
MTGA
OG
ITGA
TP
FMG
Superior temporal plane
Med
Post
Ant
Lat
TP
HGPM
PP
HGAL
PT
Ventral view
Lat
Post
Ant
Med
MTGP
MTGA
ITGM
ITGA
MOG
IOG
TP
FG
PHG
OG
LingG
GR
FMG
Mesial view
ParaCL
SPL
PMC
PCC/preCun
SFG
CingM
Cun
ACC
LingG
SubcG
GR
PHG
FG
OP
TP
Sup
Ant
Post
Inf
b Left hemisphere ($N_{subjects}$ = 24, n_{sites} = 3278)
Right hemisphere ($N_{subjects}$ = 22, n_{sites} = 3209)
z_{MNI} (mm)
x_{MNI} (mm)
y_{MNI} (mm)
ROI groups:
Auditory core
Auditory non-core
Auditory-related
Prefrontal
Sensorimotor
Other
c Regions of interest
Auditory core:
HGPM
Auditory non-core:
HGAL
PT
PP
STGP
STGM
Auditory-related:
STGA
InsP*
STSU*
STSL*
MTGP
MTGM
MTGA
SMG
AGP
AGA
Prefrontal:
IFGop
IFGtr
IFGor
MFG
SFG
ACC
OG
TFG
FMG
Sensorimotor:
dPreCG
dPostCG
vPreCG
vPostCG
ParaCL
Other:
PMC
CingM
PCC/preCun
PHG
FG
ITGP
ITGM
ITGA
TP
InsA*
fOperc*
pOperc*
GR
SubcG
SPL
Cun
LingG
OP
SOG
MOG
IOG
Amyg*
Hipp*
Put*
GP*
Caud*
SubInn*
vStr*
*not pictured

122

Figure 1. ROIs and electrode coverage in all 46 subjects. **a:** ROI parcellation scheme. **b:** Locations of recording sites, color-coded according to the ROI group, are plotted in MNI coordinate space and projected onto the Freesurfer average template brain for spatial reference. Color shades represent different ROIs within a group. Projections are shown on the lateral, top-down (superior temporal plane), ventral and mesial views (top to bottom). Recording sites over orbital, transverse frontopolar, inferior temporal gyrus and temporal pole are shown in both the lateral and the ventral view. Sites in fusiform, lingual, parahippocampal gyrus and gyrus rectus are shown in both the ventral and medial view. Sites in the frontal operculum (*n* = 21), parietal operculum (*n* = 15), amygdala (*n* = 73), hippocampus (*n* = 77), putamen (*n* = 13), globus pallidus (*n* = 1), caudate nucleus (*n* = 10), substantia innominata (*n* = 5), and ventral striatum (*n* = 2) are not shown. **c:** ROI groups. HGPM, Heschl's gyrus, posteromedial portion; HGAL, Heschl's gyrus, anterolateral portion; PT, planum temporale; PP, planum polare; STGP, superior temporal gyrus, posterior portion; STGM, superior temporal gyrus, middle portion; STGA, superior temporal gyrus, anterior portion; InsP, posterior insula; STSU, superior temporal sulcus, upper bank; STSL, superior temporal sulcus, lower bank; MTGP, middle temporal gyrus, posterior portion; MTGM, middle temporal gyrus, middle portion; mTGA, Middle temporal gyrus, anterior portion; SMG, supramarginal gyrus; AGP, angular gyrus, posterior portion; AGA, angular gyrus, anterior portion; IFGop, inferior frontal gyrus, pars opercularis; IFGtr, inferior frontal gyrus, pars triangularis; IFGor, inferior frontal gyrus, pars orbitalis; MFG, middle frontal gyrus; SFG, superior frontal gyrus; ACC, anterior cingulate cortex; OG, orbital gyri; TFG, transverse frontopolar gyrus; FMG, frontomarginal gyrus; dPreCG, precentral gyrus, dorsal portion; dPostCG, postcentral gyrus, dorsal portion; vPreCG, precentral gyrus, ventral portion; vPostCG, postcentral gyrus, ventral portion; ParaCL, paracentral lobule; PMC, premotor cortex; CingM, cingulate gyrus, middle portion; PCC/preCun, cingulate gyrus, posterior portion / precuneus; PHG, parahippocampal gyrus; FG, fusiform gyrus; ITGP, inferior temporal gyrus, posterior portion; ITGM, inferior temporal gyrus, middle portion; ITGA, inferior temporal gyrus, anterior portion; TP, temporal pole; InsA, anterior insula; fOperc, frontal operculum; pOperc, parietal operculum; GR, gyrus rectus; SubcG, subcallosal gyrus; SPL, intraparietal sulcus / superior parietal lobule; Cun, cuneus; LingG, lingual gyrus; OP, occipital pole; SOG, superior occipital gyrus; MOG, middle occipital gyrus; IOG, inferior occipital gyrus; Amyg, amygdala; Hipp, hippocampus; Put, putamen; GP, globus pallidus; Caud, caudate nucleus ; SubInn, substantia innominata ; vStr, ventral striatum.

Supplementary Table 1. Subject demographics.

Subject	Age	Sex	Handedness	Language dominance	Subdural arrays	Seizure focus
L275	30	M	R	L	Y	L lateral ventral temporal, R posterior ventral frontal
L282	40	M	R	?	N	L posterior superior temporal, L posterior lateral ventral frontal
L287	18	M	R	?	Y	L parietal
R288	21	M	R	L	Y	R temporal pole
L292	50	F	L	R	Y	L medial temporal
R294	35	M	R	?	Y	R dorsal frontal pole
L307	32	M	R	L	Y	L posterior insula
R316	31	F	R	?	Y	R medial temporal
R320	51	F	R	?	Y	R medial temporal
R322	28	F	R	?	Y	R posterior medial frontal
R329	20	M	R	?	Y	R medial frontal
R334	39	M	L	L	Y	R posterior medial temporal
R335	32	M	R	L	Y	bilateral medial temporal
L357	36	M	R	L	Y	L medial temporal
L362	59	M	R	B	Y	bilateral multiple locations
R369	30	M	R	L	Y	R medial temporal
L372	34	M	R	L	Y	L temporal pole
R376	48	F	R	L	Y	R medial temporal
R399	22	F	R	L	Y	R temporal (uncertain medial & neocortical)
L400	59	F	R	L	Y	L amygdala (medial temporal)
L403	56	F	R	L	Y	L medial temporal
L405	19	M	R	L	Y	L frontal (posterior lateral)
L409	31	F	R	L	Y	L medial temporal, L temporal pole
R413	22	M	L	R	Y	R medial temporal
L416	33	M	B	L	Y	L ventral occipital, L lateral temporal
R418	25	F	R	L	Y	R temporal (medial & lateral posterior cortex)
L423	51	M	R	L	Y	L medial temporal
L425	52	M	L	?	Y	L medial temporal
R429	32	F	R	L	Y	R medial temporal and temporal pole
R434	39	F	R	L	Y	R medial temporal
L439	37	M	R	L	N	R medial frontal (posterior dorsal)
L442	33	F	R	L	Y	multifocal L frontal, temporal, parietal
R456	31	M	L	?	Y	R medial temporal, R posterior lateral superior temporal
L457	18	M	R	?	N	L medial temporal
R458	23	M	R	L	N	R temporal (middle & posterior lateral)
L460	52	M	R	L	Y	L hippocampus (medial temporal)
L477	23	F	R	L	Y	L parietal
L514	46	M	R	L	N	L insula (anterior)
R515	21	F	R	L	N	R medial temporal
R524	18	M	L	L	N	R medial temporal, L medial temporal
L525	46	F	R	L	Y	Bilateral multifocal (predominantly L frontal & temporal)
R532	42	F	R	L	Y	R ventral frontal (posterior)
L538	18	F	R	L	N	L insula and orbitofrontal
R559	27	F	R	L	N	R inferior frontal (middle - posterior)
R567	33	M	R	?	N	R insula
L585	39	F	R	L	Y	L medial temporal

Supplementary Table 2. ROIs and electrode coverage.

ROI group	ROI	ROI abbreviation	Overall average embedding		Language dominance		fMRI	
			$N_{subjects}$	n_{sites}	$N_{subjects}$	n_{sites}	$N_{subjects}$	n_{sites}
Auditory core	Heschl's gyrus, posteromedial portion	HGPM	**35**	**168**	**33**	**157**	**10**	**49**
Auditory non-core	Heschl's gyrus, anterolateral portion	HGAL	**29**	**109**	**28**	**104**	**7**	**22**
	Planum temporale	PT	**20**	**61**	**18**	**56**	**8**	**22**
	Planum polare	PP	**23**	**49**	**21**	**47**	**8**	**22**
	Superior temporal gyrus, posterior portion	STGP	**36**	**352**	**34**	**313**	**10**	**83**
	Superior temporal gyrus, middle portion	STGM	**34**	**223**	**32**	**195**	**10**	**53**
Auditory-related	Superior temporal gyrus, anterior portion	STGA	**28**	**64**	**26**	**60**	**8**	**19**
	Posterior insula	InsP	**30**	**87**	**29**	**85**	**9**	**15**
	Superior temporal sulcus, upper bank	STSU	**23**	**107**	*22*	*106*	*4*	*13*
	Superior temporal sulcus, lower bank	STSL	**24**	**75**	**24**	**75**	**5**	**17**
	Middle temporal gyrus, posterior portion	MTGP	**36**	**410**	**34**	**376**	**10**	**98**
	Middle temporal gyrus, middle portion	MTGM	**37**	**278**	**35**	**250**	**10**	**74**
	Middle temporal gyrus, anterior portion	MTGA	**32**	**110**	**30**	**100**	**9**	**34**
	Supramarginal gyrus	SMG	**37**	**351**	**34**	**309**	**10**	**93**
	Angular gyrus, posterior portion	AGP	**15**	**66**	*14*	*62*	**6**	**27**
	Angular gyrus, anterior portion	AGA	**29**	**156**	**27**	**140**	**9**	**65**
Prefrontal	Inferior frontal gyrus, pars opercularis	IFGop	**35**	**109**	**33**	**101**	**10**	**32**
	Inferior frontal gyrus, pars triangularis	IFGtr	**37**	**184**	**35**	**176**	**9**	**48**
	Inferior frontal gyrus, pars orbitalis	IFGor	**18**	**42**	**17**	**38**	**4**	**9**
	Middle frontal gyrus	MFG	**40**	**489**	**37**	**443**	**9**	**106**
	Superior frontal gyrus	SFG	**23**	**201**	*21*	*192*	*5*	*59*
	Anterior cingulate cortex	ACC	**23**	**38**	*21*	*36*	**5**	**6**
	Orbital gyri	OG	**40**	**369**	**38**	**353**	**10**	**104**
	Transverse frontopolar gyrus	TFG	**20**	**85**	*20*	*85*	**7**	**23**
	Frontomarginal gyrus	FMG	*4*	*9*	*4*	*9*	*0*	*0*
Sensorimotor	Precentral gyrus, dorsal portion	dPreCG	**28**	**96**	**27**	**93**	**7**	**19**
	Postcentral gyrus, dorsal portion	dPostCG	**24**	**91**	*22*	*80*	**4**	**14**
	Precentral gyrus, ventral portion	vPreCG	**39**	**215**	**37**	**202**	**10**	**48**
	Postcentral gyrus, ventral portion	vPostCG	**35**	**184**	**32**	**170**	**9**	**47**
	Paracentral lobule	ParaCL	*5*	*12*	*5*	*12*	*0*	*0*
Other	Premotor cortex	PMC	**39**	**166**	**36**	**146**	**9**	**35**
	Cingulate gyrus, middle portion	CingM	**19**	**34**	*16*	*29*	**5**	**9**
	Cingulate gyrus, posterior portion / Precuneus	PCC/preCun	**18**	**77**	*15*	*68*	*2*	*5*
	Parahippocampal gyrus	PHG	**28**	**109**	**27**	**107**	**8**	**24**
	Fusiform gyrus	FG	**33**	**152**	**31**	**147**	**9**	**25**
	Inferior temporal gyrus, posterior portion	ITGP	**24**	**85**	**23**	**83**	**8**	**24**
	Inferior temporal gyrus, middle portion	ITGM	**30**	**109**	**29**	**107**	**7**	**22**
	Inferior temporal gyrus, anterior portion	ITGA	**28**	**111**	**26**	**102**	**8**	**38**
	Temporal pole	TP	**33**	**281**	**31**	**259**	**10**	**77**
	Anterior insula	InsA	**26**	**58**	**24**	**55**	**9**	**16**
	Frontal operculum	fOperc	**13**	**21**	*12*	*20*	*4*	*7*
	Parietal operculum	pOperc	*5*	*15*	*5*	*15*	*1*	*2*
	Gyrus rectus	GR	**30**	**62**	**29**	**60**	**9**	**15**
	Subcallosal gyrus	SubcG	*5*	*8*	*4*	*7*	*1*	*1*
	Intraparietal sulcus / Superior parietal lobule	SPL	**15**	**91**	**13**	**80**	**4**	**13**
	Cuneus	Cun	*4*	*7*	*4*	*7*	*2*	*3*
	Lingual gyrus	LingG	*10*	*24*	*10*	*24*	*3*	*5*
	Occipital pole	OP	*2*	*4*	*2*	*4*	*0*	*0*
	Superior occipital gyrus	SOG	*4*	*9*	*3*	*7*	*0*	*0*
	Middle occipital gyrus	MOG	**18**	**73**	*17*	*64*	**5**	**23**
	Inferior occipital gyrus	IOG	*8*	*20*	*8*	*20*	*3*	*8*
	Amygdala	Amyg	**29**	**73**	**28**	**72**	*6*	*19*
	Hippocampus	Hipp	**29**	**77**	**28**	**76**	**6**	**15**
	Putamen	Put	*8*	*13*	*8*	*13*	*3*	*4*
	Globus pallidus	GP	*1*	*1*	*0*	*0*	*1*	*1*
	Caudate nucleus	Caud	*5*	*10*	*5*	*10*	*0*	*0*
	Substantia innominata	SubInn	*2*	*5*	*2*	*5*	*2*	*5*
	Ventral striatum	vStr	*1*	*2*	*1*	*2*	*1*	*2*
Total			46	6487	43	6014	10	1619

Subject and site numbers that were not included in group averages are denoted in *gray italics*.

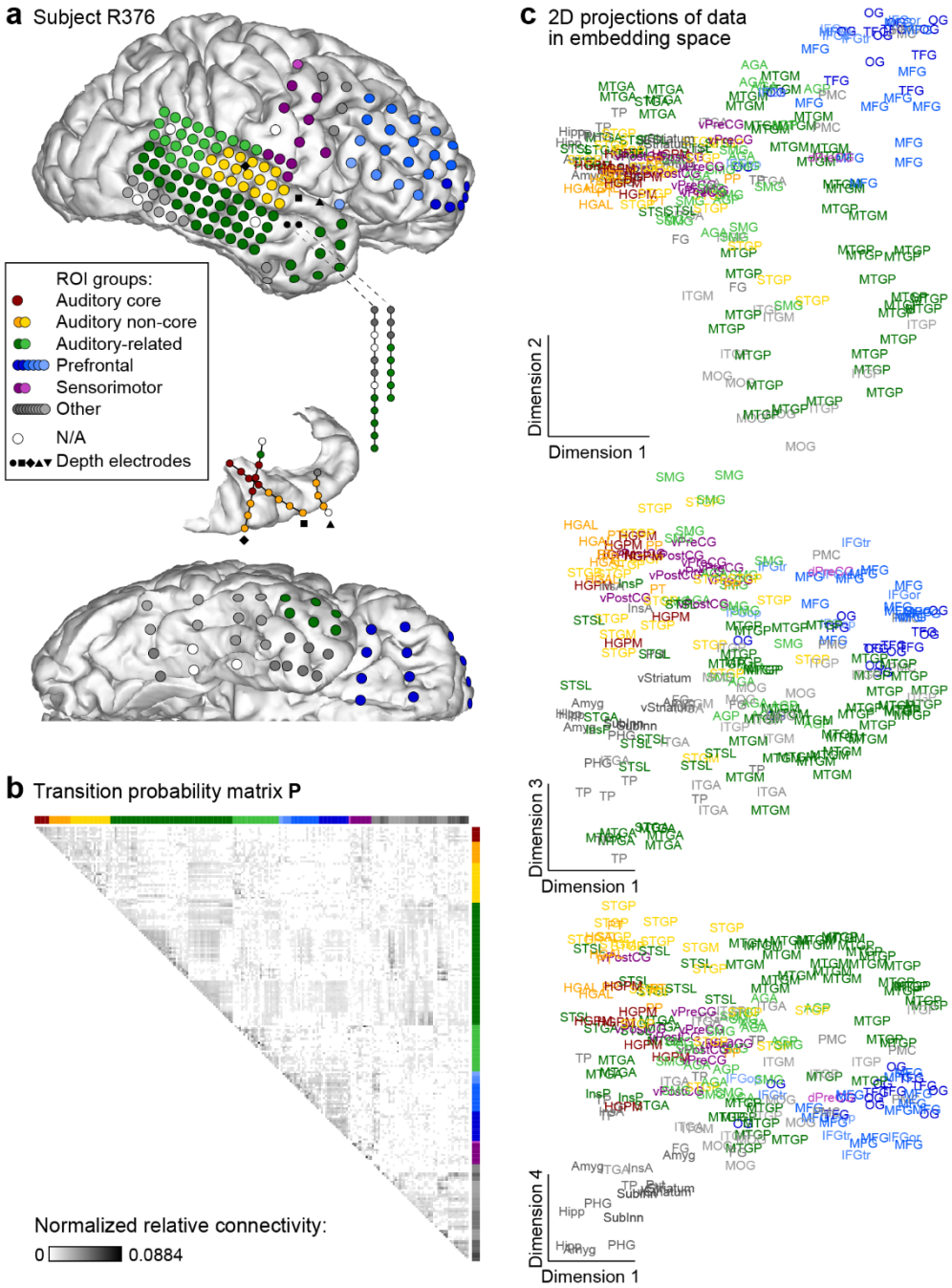

Figure 2. Functional geometry of cortical networks revealed by DME in a single subject (R376). **a:** Electrode coverage. **b:** Normalized adjacency matrix. **c:** Data plotted in the 1st and 2nd, 1st and 3rd, and 1st and 4th dimensions of embedding space (top to bottom). Two points that are close in embedding space are similarly connected to the rest of the network, and thus assumed to be functionally similar. Scale bar: 0.03.

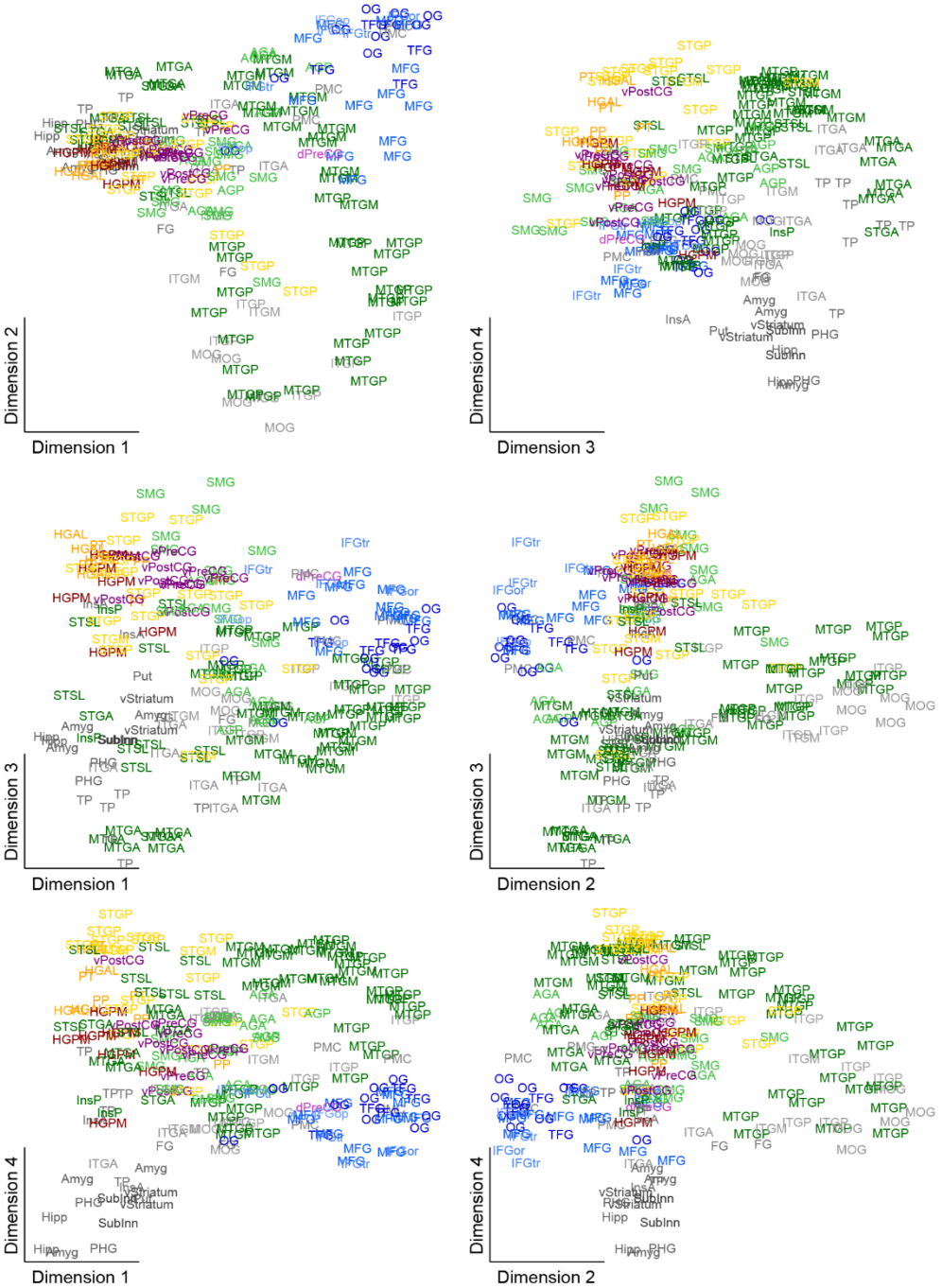

Supplementary Figure 1. Embedding plots in subject R376 plotted in four dimensions. Scale bar: 0.04.

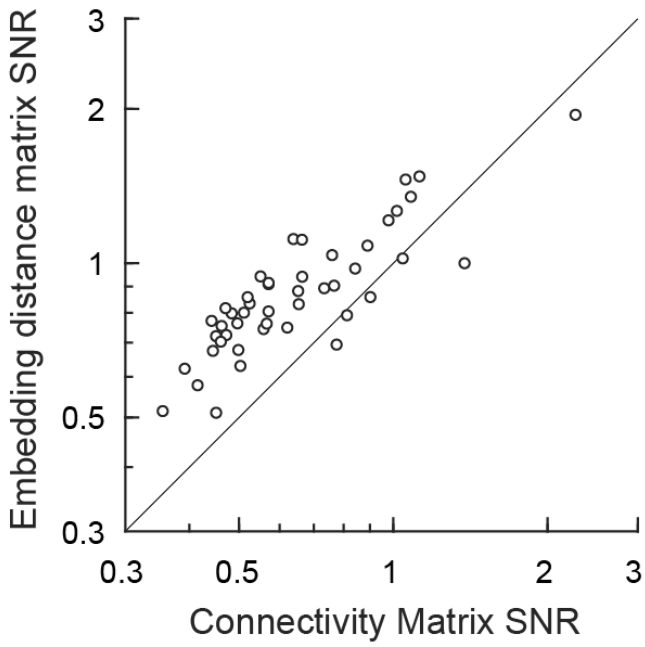

Supplementary Figure 2. Comparison of signal to noise ratio (SNR) for the embedding analysis versus direct analysis of functional connectivity. Each symbol corresponds to one subject. For each subject, the SNRs of embedding distances and connectivity were calculated from the recorded RS block as described in Methods. In most subjects, the embedding analysis exhibited superior noise characteristics compared to direct analysis of connectivity.

To pool data across subjects with variable electrode coverage, ROI-by-ROI connectivity matrices were computed for each subject and averaged across subjects. The resulting mean **P** for the entire dataset (N = 46) is shown in Figure 3a. The eigenvalue spectrum $|\lambda_i|$ of **P** featured an inflection point for i>4, indicating that the first four dimensions of embedding space provided a reasonable approximation for discerning the community structure of the data (Fig. 3a, inset). This representation is shown in Figure 3b, where three different views of the data are plotted for the first 4 dimensions of embedding space (see Supplementary Fig. 3 for three additional views and Supplementary Movies 1 and 2 for three-dimensional representations).

The data of Figure 3b are a graphical representation of the functional geometry of auditory cortical networks and all other simultaneously sampled brain structures. Functionally related ROIs tended to cluster within embedding space. For example, canonical auditory cortical and PFC ROIs were at opposite ends of dimension 1, and parietal and limbic ROIs were at opposite ends of dimension 2. By contrast, some ROIs (e.g., STGA, MTGA, MTGM) were situated in the interior of the data cloud.

Using a functional connectivity metric that discards components exactly in phase between two brain regions mitigates the influence of volume conduction[36]. However, brain areas that are anatomically close to each other are often densely connected[37-41]. Thus, anatomical proximity is expected to contribute to the observed functional geometry. Auditory cortical ROIs followed this rule and clustered together with one notable exception. Planum polare (PP), located immediately anterior to HG on the superior temporal plane, was located at a considerable distance from the rest of auditory cortical ROIs along dimension 2 in embedding space (Fig. 3b, lower left corner of the upper panel). Separation in embedding space was also observed along specific dimensions between STGA and STGM, between TP and the rest of the anterior temporal lobe, and between InsA and InsP. Overall, physical proximity explained an average of 15% of the variance in embedding distance (mean adjusted r^2 = 0.15 for regressions between physical and embedding Euclidean distance, calculated separately for each ROI). Thus, the embedding representation is informative in elucidating the functional organization of the sampled networks beyond anatomical proximity.

The grouping of the canonical auditory cortex is apparent in this representation, as STGM, STGP, PT, and HGAL were all in close proximity to HGPM. The same was true for STSU, which was positioned in proximity to canonical auditory cortical ROIs. This relationship did not hold, however, for STSL. Indeed, in embedding space STSU was significantly closer to canonical auditory cortex (HGPM, HGAL, PT, PP, STGP, STGM) than STSL (p=0.002).

The separation of the lower and upper banks of the superior temporal sulcus (STSL, STSU) is consistent with functional differences in their response properties reported recently[9]. In that work, responses in STSL, but not STSU, were predictive of performance on a semantic categorization task. This suggests that in embedding space, STSL would be closer to regions involved in semantic processing compared to STSU. This hypothesis was tested by comparing the distance in embedding space between ROIs classically described as contributing to semantic

processing (IFGop, IFGtr, IFGor, TP, STGA, MTGA, ITGA, MTGP, ITGP, AGA, AGP, SMG;[42-44]) and STSL versus STSU. A permutation analysis to test statistical significance revealed that STSL was indeed closer to these semantic processing ROIs compared to STSU (p=0.010).

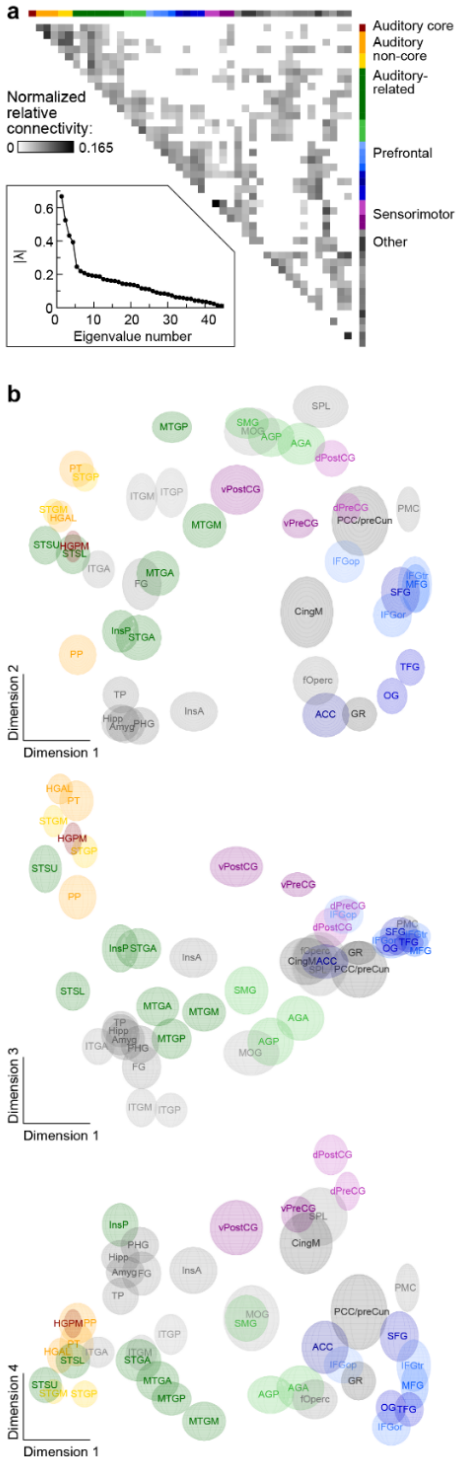

Figure 3. Summary of functional geometry of cortical networks via DME. **a**: Average normalized adjacency matrix. **Inset:** Eigenvalue spectrum. **b:** Data plotted in the 1st and 2nd, 1st and 3rd, and 1st and 4th dimensions of embedding space (top to bottom). Variance estimates on the locations of each ROI in embedding space were obtained via bootstrapping and are represented by the size of the ellipsoid for each ROI. Scale bar: 0.1.

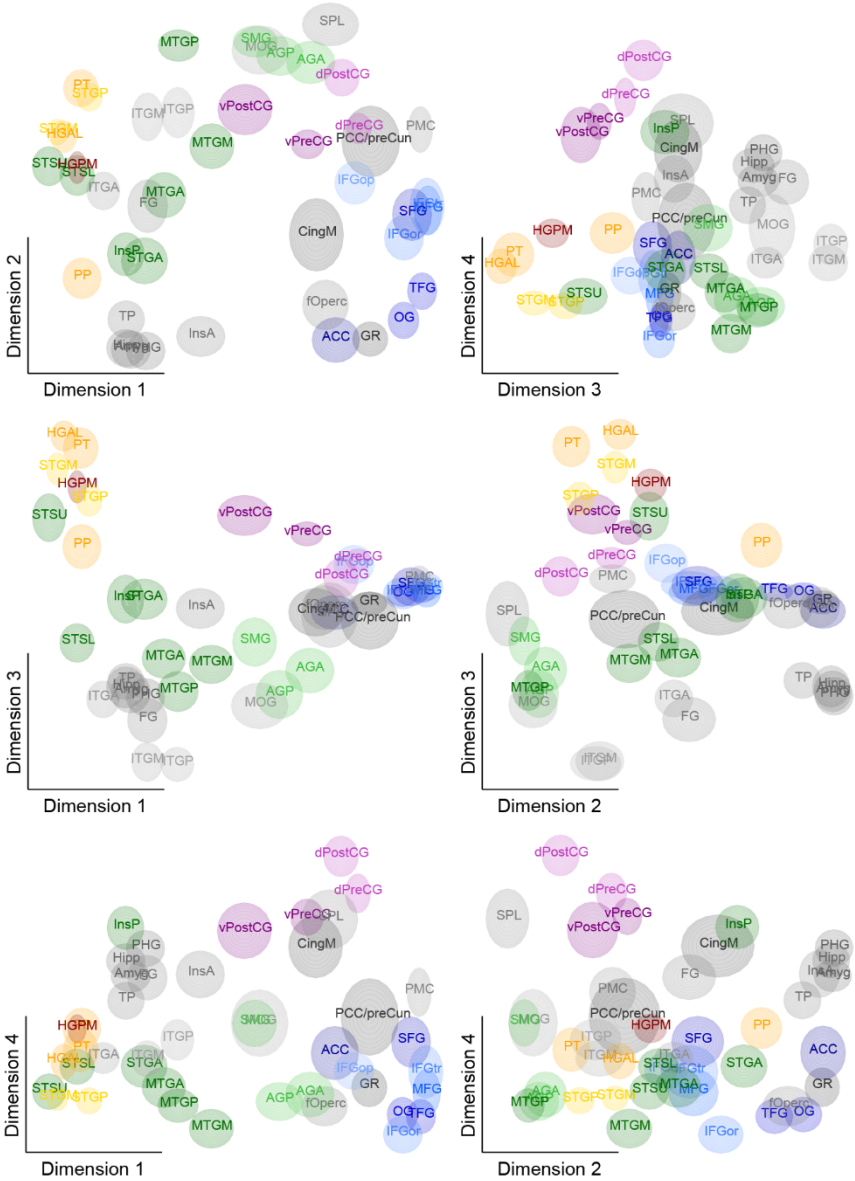

Supplementary Figure 3. Average embedding plots in four dimensions. Scale bar: 0.1.

221 InsP responds robustly to acoustic stimuli[7], consistent with suggestions that a portion of this
222 area should be considered an auditory region[45]. Indeed, InsP is capable of phase locking to
223 fundamental frequency of male voices (F0>100 Hz) in a manner akin to that seen in HGPM,
224 (Steinschneider et al., 2013; Zhang et al., 2019), suggesting direct inputs from the auditory
225 thalamus. However, in the present data InsP was functionally segregated from early auditory
226 cortical regions and was situated between early auditory and limbic ROIs. This finding was
227 consistent with the broader role of InsP in both exteroceptive processing across multiple
228 sensory modalities as well as interoception[46, 47].

229 Figure 3b also characterizes the temporal and parietal ROIs outside canonical auditory cortex
230 that are nonetheless part of the extended auditory network, including elements of the dorsal
231 and ventral processing streams. These areas, labeled here as 'auditory-related' ROIs and
232 denoted by shades of green in Figure 3b, were distributed along a considerable extent of all
233 four dimensions, consistent with functional heterogeneity of these regions and their
234 involvement in multimodal integration[48].

235 So far, the results of analyses have been presented at a single spatial scale, corresponding to *t* =
236 1, which emphasizes local network structure. Analysis of data in embedding space
237 corresponding to *t* = 5 is presented in Supplementary Figure 4. The dominant structure in the
238 data is governed by dimension 1, with early auditory ROIs at one end and PFC ROIs at the other.
239 This indicates that the functional distance between these two groups of ROIs is the most
240 prominent of all organizational features in the data.

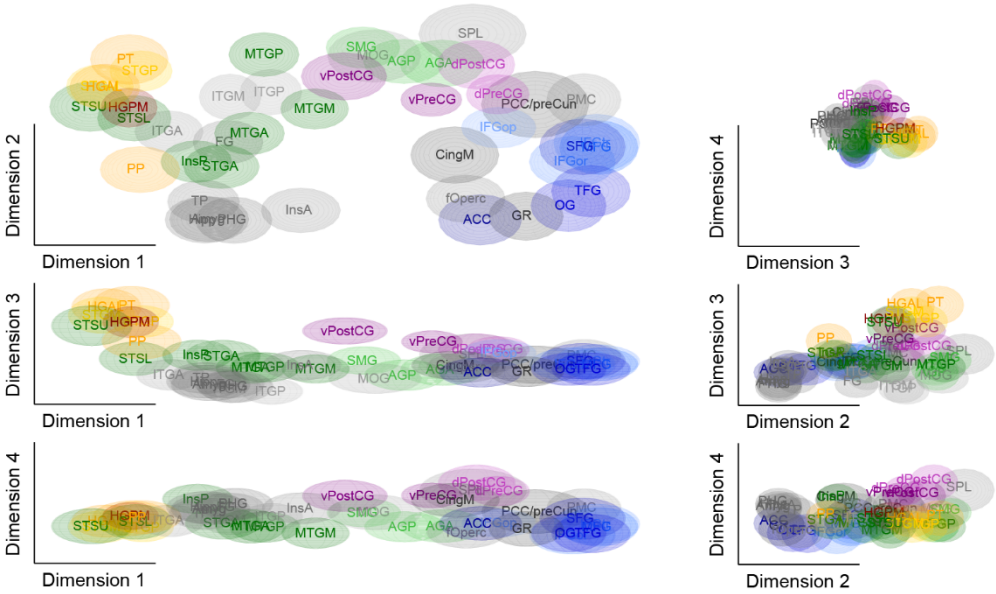

241

242 **Supplementary Figure 4.** Analysis of data at a larger spatial scale. Data plotted in embedding space for *t*
243 = 5. Data plotted in the first four dimensions of embedding space. Scale bar: 0.01.

The grouping structure of ROIs presented in Figure 3 was characterized by applying hierarchical clustering to the first four dimensions of the embedded data (Fig. 4). The ROIs considered in the present study segregated into several clusters. Canonical auditory ROIs (HGPM, HGAL, PT, STGP, STGM) formed a clearly delineated 'Auditory' cluster that also included the auditory-related ROI STSU. Another major cluster could be identified that included ROIs traditionally considered part of the limbic system (PHG, Amyg and Hipp), anterior temporal lobe ROIs (TP, STGA, PP), and both subdivisions of the insula. This cluster is labeled 'Limbic' in Figure 4. Next, ROIs typically considered part of the ventral and dorsal streams of sound processing segregated into two clusters, followed by (primarily prefrontal) ROIs typically considered as being involved in executive functions and those involved in sensorimotor functions (labeled 'Executive' and 'Action' in Fig. 4). Thus, the hierarchical clustering analysis revealed a segregation of ROIs in embedding space that aligns with known functional differentiation of brain regions.

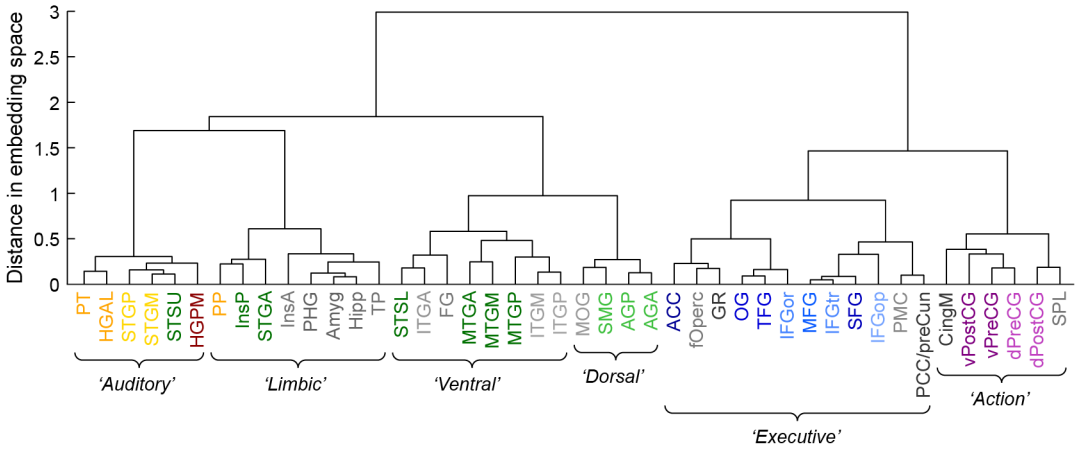

Figure 4. Hierarchical clustering of embedding data. Dendrogram showing linkages between ROI groups identified using agglomerative clustering.

Critically important to understanding the topology of brain networks is the identification of network nodes that serve as 'global hubs', i.e., nodes that are particularly important for integrating and regulating information flow in the network by virtue of their centrality and strong connectivity. DME analysis can identify global hubs, as the closer an ROI is to the center of the data cloud in embedding space, the more equal is its connectivity to the rest of the network. This scenario is schematically illustrated in Figure 5a, which depicts a network consisting of five ROIs, with one central ROI serving as a global hub (shown in green in Fig. 5a). The network structure can also be represented as an adjacency matrix, wherein the hub ROI has strong connectivity with other ROIs (Fig. 5a, middle panel). In embedding space, this hub ROI occupies a central location, with the other four ROIs serving as spokes (Fig. 5a, right panel).

A node's distance from the center of embedding space is correlated with the variance of its connectivity to the rest of the network, rather than with the mean of its connectivity. Thus, a node can appear at a central location in embedding space if equally but weakly connected to the rest of the network. By contrast, a node strongly connected to a small number of other nodes ('local hub') will have high mean connectivity but will be distant from the center of embedding space. Combining distance from the center of the data cloud with mean connectivity allows for classification of ROIs as global versus local hubs and for distinguishing hubs from spokes and central nodes that have relatively weak overall connectivity to the rest of the network ('bridge'). This is illustrated in Figure 5b, which shows the average connectivity versus distance to the centroid of the data cloud in embedding space for the ROIs from the average embedding in Figure 3c. In the network of sampled ROIs, anterior temporal lobe ROIs (MTGA, MTGM, STGA) appear as global hubs (upper left quadrant of the plot). These three ROIs lie outside 2 standard deviations from the mean distance to center of embedding space and connectivity (outside dashed ellipse). To a lesser extent, ROIs such as STSU and OG demonstrate high connectivity but are located at a greater distance from the center of embedding space and can thus be considered local hubs. Primary sensory and motor regions and canonical auditory ROIs (with the exception of PP) tend to behave as spokes, occupying the lower right quadrant of the graph. Finally, the ROIs in the lower left quadrant can be considered bridges between isolated clusters of ROIs in the sampled network, characterized by more selective connectivity patterns. Thus, DME can identify topological features critical to information flow within cortical networks.

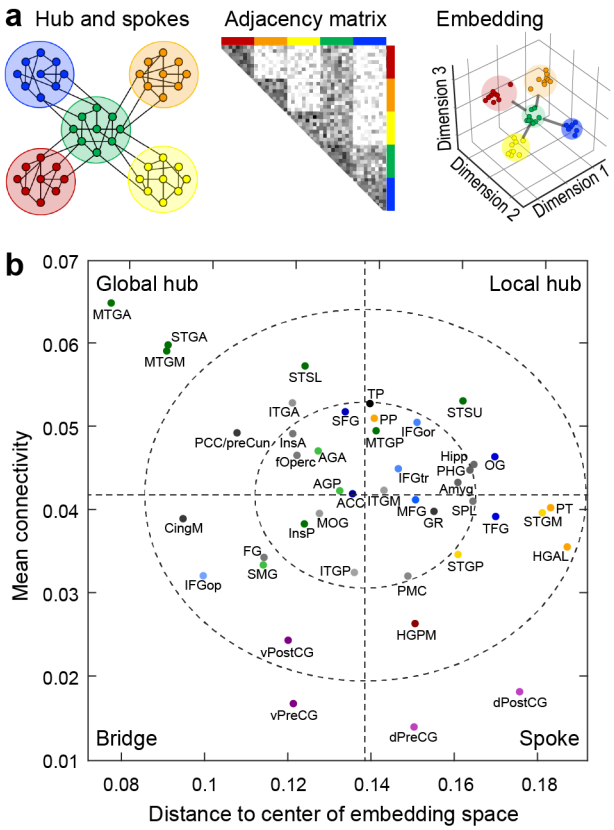

Figure 5. Identification of network hubs. **a:** Schematic example illustrating the central positioning of global hubs in embedding space. **b:** ROIs from average embedding are plotted according to their mean connectivity to the rest of the network versus their distance to the centroid of the data cloud in the first four dimensions of embedding space. Dashed lines denote across-ROI means. Dashed ellipses represent 1 and 2 standard deviations from the mean.

Hemispheric differences

Speech and language networks are lateralized in the human brain, with nearly all right-handed and most left-handed individuals left hemisphere language-dominant[49]. However, functional imaging and electrophysiology studies indicate that both hemispheres are activated during speech processing and comprehension tasks (reviewed in[13, 26, 50, 51]). The extent to which functional specialization is reflected in asymmetries in the organization of auditory networks is not clear. We explored this issue by comparing the geometry of cortical networks derived from subjects with implants in the language-dominant (N = 22) versus language–non-dominant (N = 21) hemisphere. The average embeddings are illustrated in Supplementary Figure 5 for the combined dataset, subjects with electrodes implanted in the language dominant hemisphere and in the language non-dominant hemisphere (panels a, b and c, respectively).

Visual inspection of the data in embedding space suggests a symmetric functional organization of ROIs. To test for quantitative differences in this organization, we calculated pairwise inter-ROI distances in embedding space for all ROIs in the analysis (Fig. 6, left panel). The inter-ROI distances in embedding space for dominant versus non-dominant hemispheres were highly correlated (r = 0.77), with no obvious outliers. Furthermore, this was true specifically for distances between ROIs postulated to be involved in speech and language comprehension and production (PT, PP, STSL, STGP, STGM, STGA, SMG, AGA, PMC, PreCG, IFGop, IFGtr)[16, 52, 53] (Fig. 6, right panel).

Permutation analysis indicated that neither the positions of ROIs in embedding space nor the pairwise distances between ROIs were significantly different between dominant and non-dominant hemispheres (after FDR correction all p-values >0.05). Thus, hemispheric asymmetry of functional organization of speech and language networks was not detectable in RS connectivity.

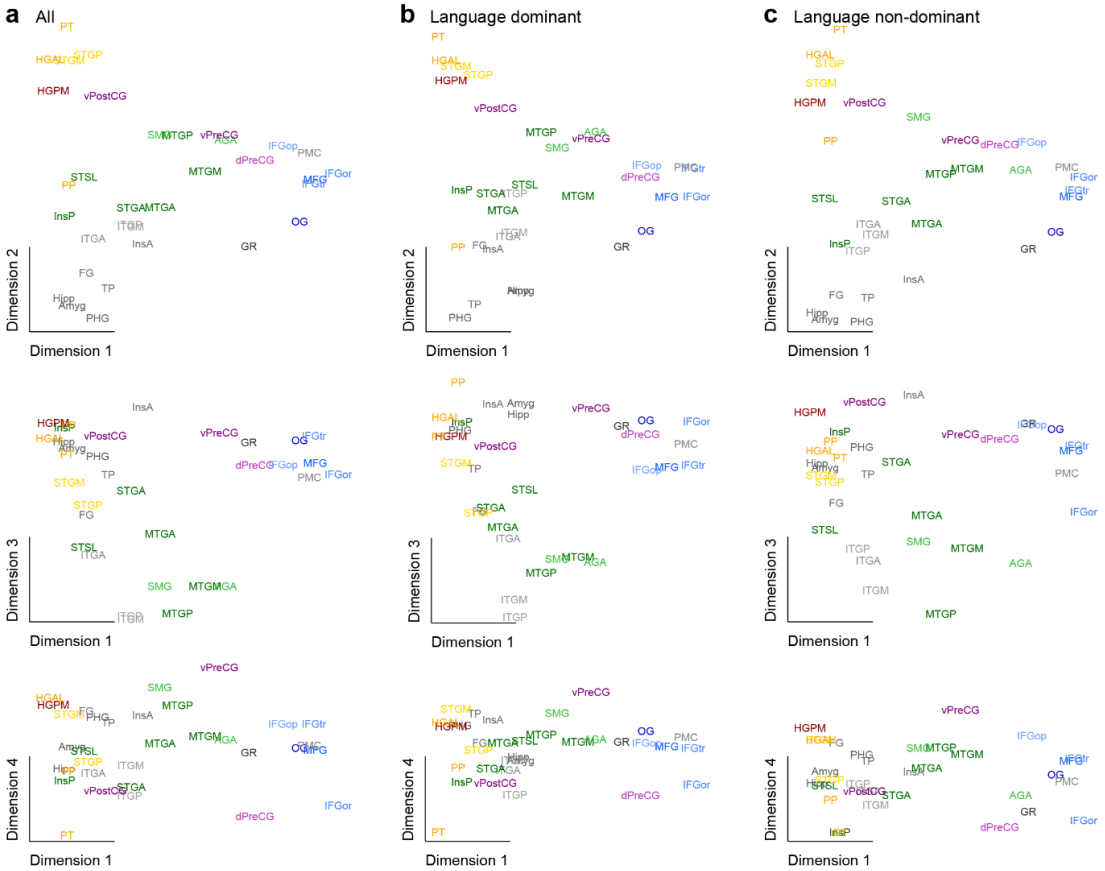

Supplementary Figure 5. Auditory networks do not differ between hemispheres. A-C. Data plotted in the first 4 dimensions of embedding space for all dominant and non-dominant subjects (A), just dominant (B), and just non-dominant (C). Scale bar: 0.1. D. Inter-ROI distances in embedding space for non-dominant versus dominant hemisphere subjects.

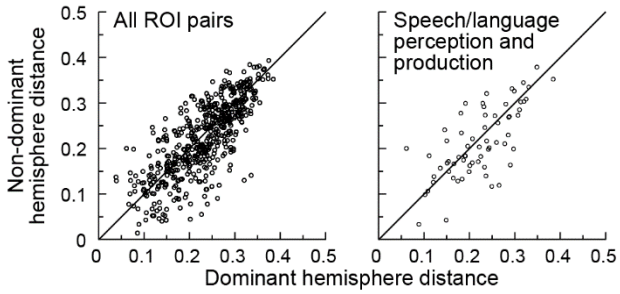

Figure 6. Auditory networks do not differ between hemispheres. Inter-ROI distances in embedding space for non-dominant versus dominant hemisphere subjects. Pairwise distances between all ROIs and between ROIs involved in speech and language perception and production (PT, PP, STSL, STGP, STGM, STGA, SMG, AGA, PMC, PreCG, IFGop, IFGtr) are shown in the left and right panel, respectively. Note that after splitting the data into the two subsets (dominant and non-dominant) STSU did not meet the inclusion criteria for analysis presented in the right panel (see Methods, Supplementary Table 2).

Stability of functional geometry across frequency band and connectivity measures

So far, embeddings have been based on functional connectivity measured as gamma-band power envelope correlations.

To examine whether the results could be generalized across iEEG frequency bands and functional connectivity measures, inter-ROI distances in embedding space were compared for envelope correlations and weighted phase lag index (wPLI) from different frequency bands (Supplementary Fig. 6a). For power envelope correlations, relationships between inter-ROI distances were especially strong for adjacent bands ($r \geq 0.83$), and the correlations were high even for non-adjacent bands ($r \geq 0.72$). For wPLI, relationships were slightly weaker, but still exhibited consistency across frequency bands (0.59-0.79). Finally, correlations were comparably high even across the two functional connectivity measures (0.58-0.78). Thus, the choice of gamma band power envelope as the principal measure of functional connectivity was representative of overall organizational features of cortical networks as captured by the embedding analysis.

Inter-subject variability in the position of ROIs in embedding space did exhibit frequency- and measure-dependence. This was analyzed using bootstrapping across subjects to estimate the positional uncertainty of ROIs in embedding space (represented in the sizes of the ellipsoids in Figure 3b). The mean uncertainty across all ROIs for each band and measure was computed, as illustrated in Supplementary Figure 6b. There was little difference in the uncertainty for the three higher frequency bands used for power envelope correlations (beta, gamma and high gamma), but the uncertainty was larger for lower frequency bands (theta and alpha) and for wPLI. The analyses of Supplementary Figure 5 suggest that gamma power envelope correlations are a reasonable metric for exploring functional geometry and exhibit noise properties as good or superior to other bands and to wPLI.

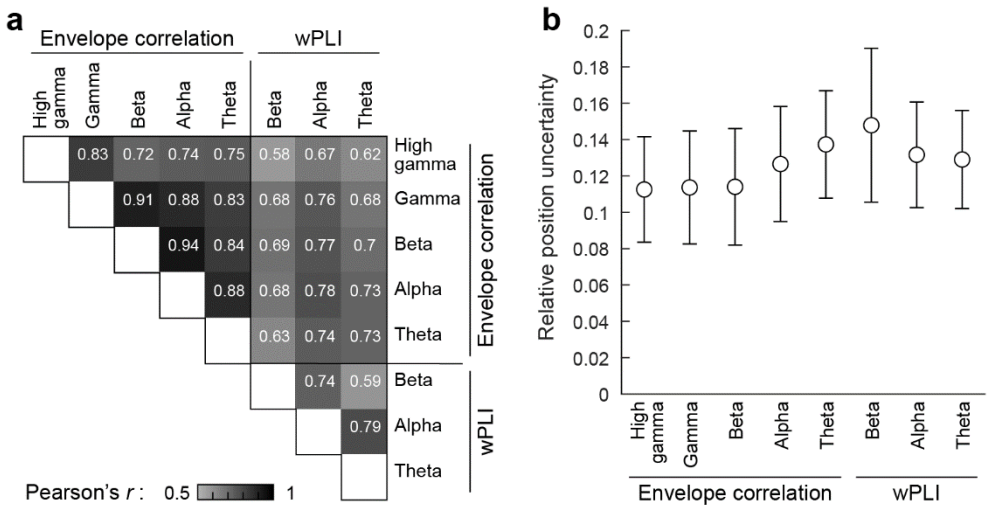

Supplementary Figure 6. Comparison of embedding results across frequency bands and functional connectivity measures. **a:** Correlations of embedding distances between measures and bands. **b:** Variability of embedding positions as a function of measure and band.

Comparison to embeddings derived from RS-fMRI data

iEEG recordings sample the brain sparsely as dictated by clinical considerations. The limited extent and density of iEEG sampling is true on the scale of the entire brain, as implanted electrodes are usually confined to a single hemisphere and to specific ROIs in that hemisphere. Furthermore, within a specific ROI, coverage is sparse. To evaluate the effects of limited, non-uniform sampling on the resulting embeddings, DME was applied to RS-fMRI data available in a subset of subjects (N = 10). A prerequisite for this approach was to demonstrate the consistency of functional geometry as revealed using the two modalities in the same subset of subjects (Fig. 7). For this analysis, fMRI connectivity matrices were constructed based on RS-fMRI data from voxels located at iEEG recording sites and grouped into the same ROIs as in Figure 1.

The iEEG and fMRI embeddings averaged across subjects were qualitatively similar (Fig. 7a, b). Furthermore, the overall organization derived from this subset of subjects based on iEEG and fMRI data was consistent with that observed in the full iEEG dataset (cf. Fig. 3b). To compare iEEG and fMRI embeddings quantitatively, inter-ROI distances in the fMRI and iEEG embedding spaces were computed, and correlations between these distances were measured (Fig. 7c, d). Correlation coefficients were highest for beta-, gamma- and high gamma-band envelope (r > 0.5; Fig. 7d, line and symbols). Qualitatively similar results were found at the individual subject level as well, albeit with smaller r values (Fig. 7d, box and whiskers plot).

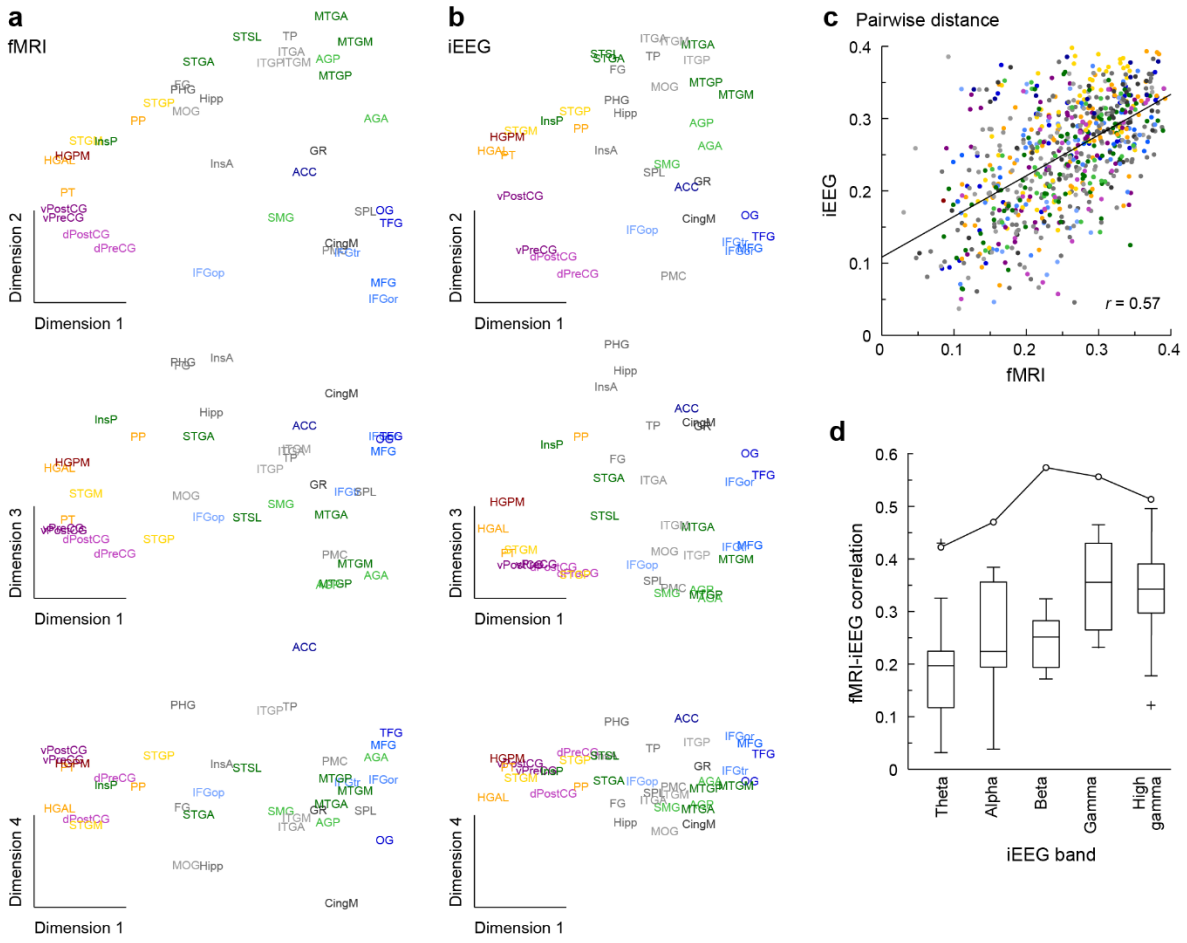

Figure 7. Comparison of iEEG and fMRI connectivity data in embedding space. **a:** Subject-averaged embeddings for iEEG (gamma band power envelope correlations). **b**: Subject-averaged embeddings for fMRI. Scale bar: 0.1. **c:** Inter-ROI embedding distances computed from the data in **a** and **b**. **d:** Summary of distance correlations at each frequency band for subject-averaged data (line and symbols) and single subjects (box and whiskers). t = 1 for all embeddings.

The similarity of embeddings derived from iEEG and fMRI data illustrated in Figure 7 indicates that fMRI data can be used to address specific questions about the effects of limited, non-uniform sampling. The first question centers on the effect of iEEG sampling only a subset of ROIs in the brain. To understand the impact of this sampling bias, the embedding derived from fMRI data measured in all cortical ROIs was compared with the embedding derived from just those ROIs sampled in each subject. For this analysis, a standard parcellation scheme developed for fMRI data (Schaefer-Yeo 400 ROIs;[54]) was used rather than the iEEG parcellation scheme introduced in Figure 1. For each subject, embeddings were derived from RS-fMRI connectivity matrices computed from all cortical ROIs ("Full fMRI", Fig. 8a, leftmost column). A subset of these ROIs that were sampled with iEEG in that subjects ["Full fMRI (iEEG subset)", Fig. 8a, 2nd column] were then retained for comparison to embeddings computed from just the fMRI data corresponding to the ROIs sampled by iEEG ["Partial fMRI (ROI level)", Fig. 8a, 3rd column]. The two embeddings were compared by computing the correlation between inter-ROI distances in the respective embedding spaces (Fig. 8b). Although the scale of the embeddings was different for the full fMRI versus partial fMRI data (because the number of dimensions was different), there was a very high correlation between the two (r = 0.94, averaged across subjects; Fig. 8c). This analysis indicates that constructing the embeddings from all cortical ROIs or just the subset of those ROIs sampled with iEEG electrodes yields comparable results.

The second question centers on the effect of representing an entire ROI by electrophysiological recordings from a sub-region of that ROI. To investigate this issue, the embeddings computed from the averages across entire ROIs in each subject ["Partial fMRI (ROI level)", Fig. 8a, 3rd column] were compared with those computed from the averages of just the fMRI voxels in the vicinity of the electrode contacts sampling each ROI ["Partial fMRI (site level)", Fig. 8a, rightmost column]. As for the comparison between iEEG and fMRI data in Figure 7, the embeddings were similar ($r > 0.5$, averaged across subjects; Fig. 8c). These data indicate that embeddings computed from a small number of locations within ROIs capture a substantial portion of the variance compared to sampling the entire ROI uniformly. Limited, non-uniform sampling within an ROI has a greater impact on estimate of functional geometry than limited sampling of the overall set of cortical ROIs. Taken together, these results indicate broad consistency between functional organization derived from iEEG and fMRI and the robustness of this approach to sparse sampling afforded by iEEG recordings.

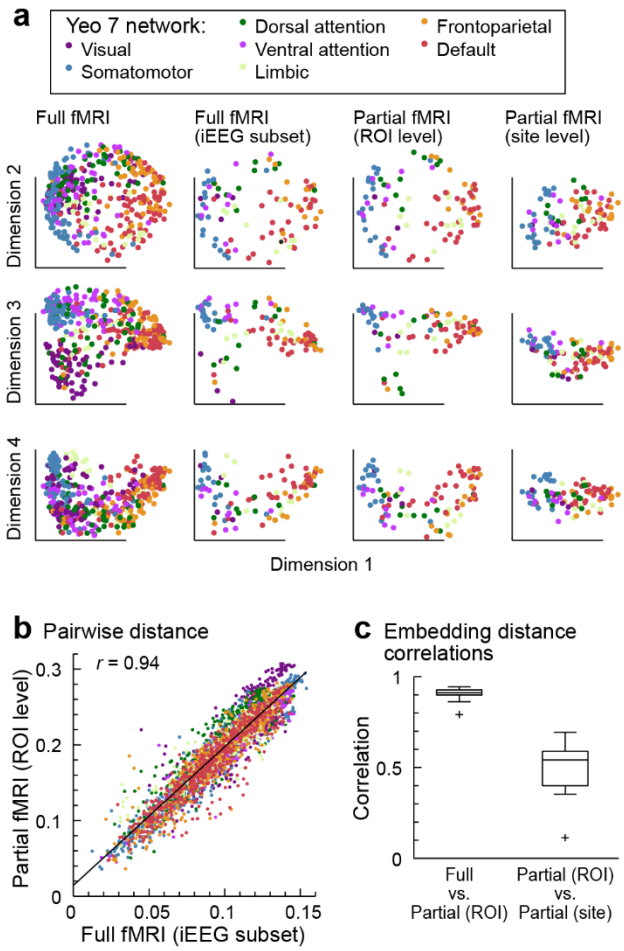

Figure 8. Effect of constructing embeddings from only a subset of ROIs in the brain. Scale bar: 0.1 (full fMRI), 0.2 (partial fMRI).

Discussion

Organization of auditory cortical networks

We have shown that DME applied to iEEG data can be used to characterize the organization of human auditory cortex and its relationship with other sampled cortical ROIs. Previous work in macaque has identified more than a dozen auditory cortical fields, with hierarchy based on cytoarchitectonics, connectivity, and response properties[55]. By contrast, there is no consensus on how auditory cortex is organized in humans, with multiple candidate parcellations based on cytoarchitectonics[56] and additional MRI-based models that rely on tonotopy or myeloarchitecture[57-59].

Our results contribute to this body of knowledge by showing that superior temporal ROIs including core auditory cortex (HGPM) and regions postulated to form human homologs of auditory belt and parabelt areas (PT, HGAL, STGP, STGM;[56, 59] clustered together in embedding space by virtue of similar connectivity to other recorded brain regions, indicating functional similarity. We could also discern hierarchical relationships within this cluster by combining embedding analysis with mean connectivity. Specifically, even though HGPM is located in close proximity to other auditory ROIs in embedding space (see Fig 3b), it exhibits weaker mean connectivity compared to these other ROIs, suggesting that it functions more like a spoke than a local hub (see Fig. 5b). This is consistent with the position of HGPM at lowest level of the auditory cortical hierarchy.

STGP had an intermediate position of between HGPM and HGAL/PT/STGM in terms of its distance to center of embedding space and mean connectivity. This finding is consistent with the interpretation of STGP as the locus of relatively early non-core auditory cortex[60, 61] and occupying a low-level position similar to HGPM in one of the multiple parallel processing streams for speech[62].

Functional differentiation between STSU and STSL

The STS is a critical node in speech and language networks linking auditory cortical structures on the superior temporal plane with higher order areas in temporal, parietal, and frontal cortex[8, 50, 52, 63-65]. In the present study, STSU, but not STSL, clustered with auditory cortical structures on the superior temporal plane and lateral STG. Although STSU is traditionally not considered part of canonical auditory cortex (but see Woods et al., 2010), the data presented here suggest that it occupies a relatively low location within the auditory cortical hierarchy. By contrast, STSL was closer in embedding space to ROIs previously shown to participate in semantic processing (IFGop, IFGtr, IFGor, TP, STGA, MTGA, ITGA, MTGP, ITGP, AGA, AGP, SMG). While the specific ROIs involved in semantic processing vary across studies, we chose to integrate multiple models[32, 42-44]. Given the number of ROIs on the list, it is unlikely that adding or subtracting several ROIs would qualitatively affect the result.

460 Previous studies have shown that the upper and lower banks of the STS (STSU and STSL) differ
461 in cytoarchitecture[66], and in the minority of imaging studies that distinguished STSU from STSL,
462 responses to speech were found to be distinct[27, 67-69]. A recent iEEG study demonstrated that
463 gamma augmentation and alpha suppression in response to speech syllables were both greater
464 and with shorter gamma onset latencies in STSU compared to STSL[9]. This study also showed
465 that responses in STSL, but not STSU, correlated with performance on a semantic categorization
466 task, consistent with the proximity of STSL to ROIs involved in semantic processing shown here.
467 Taken together, the results firmly place STSU and STSL at different levels of auditory cortical
468 hierarchy.

469

470 *Functional and theoretical framework of limbic auditory pathway*

471 Several regions that were anatomically adjacent to the auditory ROIs discussed above and
472 shown in previous studies to be activated during auditory processing were segregated from the
473 auditory cortical cluster. Our data provide evidence that these ROIs, including PP, STGA, and
474 InsP, are functionally distinct from canonical auditory cortex and likely represent higher order
475 cortical structures. Specifically, these ROIs instead were distributed in embedding space close
476 to InsA and a cluster of limbic ROIs (PHG, Amyg, Hipp, TP; see Fig. 4).

477 PP, despite its anatomical location immediately anterior to HG, has a connectivity profile
478 distinct from other regions within the STP. Instead, it is in close relationship with STGA, the
479 insula, and limbic structures. PP is unique in auditory-responsive cortex for its specific activation
480 by music, which has a strong affective component[6], as well as syntactic-level language
481 processing[5]. Similarly, InsP, despite its anatomical proximity to HGPM and similarity of
482 functional properties, was segregated from auditory ROIs. Low-level auditory information
483 represented in InsP is transformed to emphasize the affective representation of sound in InsA[7].

484 Other anterior temporal ROIs, such as STGA and TP have been positioned organizationally at
485 the pinnacle of anterior temporal lobe structures involved in semantic processing[5, 32]. These
486 regions are also associated with representation and retrieval of memories for people, social
487 language, and behaviors ('social knowledge')[70]. The latter roles are likely mediated by the tight
488 connections of the anterior temporal lobe ROIs with limbic structures that have been shown to
489 be involved in episodic, working, and emotional memory and affective sound processing[21, 23,
490 71]). Indeed, in the results presented here, TP associates tightly with limbic ROIs, consistent with
491 its association with limbic cortex[72, 73], with which it shares key features of laminar
492 cytoarchitecture. This is consistent with the strong connectivity demonstrated between
493 temporal pole and hippocampus evident in structural imaging[74]. TP has also been implicated in
494 auditory memory, based on its role in linking auditory cortex to entorhinal, perirhinal, and
495 parahippocampal cortex[75]. Consistent with this role, the clustering analysis of Figure 4 places
496 temporal pole firmly in the functional vicinity of limbic cortical structures, and also interposes
497 insular cortex, STGA and PP between this cluster and that of auditory regions.

498 Previous studies using RS-fMRI connectivity have provided evidence for an anterior temporal
499 network involving hippocampus and auditory ROIs in lateral temporal cortex[76, 77]. Information
500 underlying auditory memory and emotional auditory processing has been shown to be shared
501 between auditory cortex and limbic structures ([20-24]). The established connectivity between
502 core auditory cortex and planum polare[78], the recently reported connectivity between
503 hippocampus and planum polare[74], and indirect connections between core auditory cortex and
504 hippocampus[79] all provide further evidence for a multi-node pathway connecting auditory
505 cortex with hippocampus. These (indirect) functional and anatomical connections between
506 hippocampus and auditory cortical ROIs provide the basis for neural responses to sound stimuli
507 in hippocampus[23]. In agreement with the model in which hippocampus sends high level
508 predictions to wide areas of the brain including sensory cortex[73], a recent study using
509 intracranial electrophysiology provided evidence for effective connectivity from hippocampus
510 to auditory cortical ROIs during naturalistic story telling[80].

511 We suggest that the functional organization depicted in Figures 3 and 4, combined with
512 evidence for bidirectional information sharing between limbic and auditory cortex, merits the
513 identification of a third auditory processing stream alongside the dorsal and ventral streams[12,
514 81]. This 'limbic stream' underlies auditory contributions to emotional and episodic memory
515 processing.

516

517 *Ventral and dorsal streams linking auditory and frontal cortex*

518 Current models of cortical speech and language processing posit the existence of ventral and
519 dorsal processing streams that both originate in non-core auditory cortex, engage temporal and
520 parietal auditory-related areas, and ultimately terminate in the PMC and the IFG[12-14]. There is a
521 consensus that ventral ("what") stream forms the basis of sound-to-meaning transformations.
522 The dorsal stream has been envisioned to subserve spatial processing ("where";[12],
523 sensorimotor integration ("how";[13], and syntactic processing[14]. These streams are subserved by
524 known anatomical pathways that connect temporal, parietal and frontal regions engaged in
525 auditory processing. Specifically, inferior and middle longitudinal fasciculus and uncinate
526 fasciculus carry information along the ventral stream, whereas superior longitudinal and
527 arcuate fasciculus carry information along the dorsal stream (reviewed in[52].

528 In the present study, temporal and parietal ROIs clustered separately in a manner generally
529 consistent with this dual stream model. We observed a cluster that included STSL, MTG, and
530 ITG, consistent with the description of the ventral auditory stream proposed by Hickok and
531 Poeppel[13] and Friederici[14]. By contrast, the cluster that included SMG, AGP, and AGA aligned
532 with the dorsal processing stream as proposed by Rauschecker and Scott[12]. Association of FG
533 and MOG with the ventral and dorsal clusters, respectively, likely represents the sharing of
534 information across sensory modalities.

One of the most striking findings of this study was the separation of auditory cortex and frontal regions in embedding space. A previous fMRI-based study found a similar separation between primary sensory and executive regions[35]. In the present study, this finding was robust to the choice of the parameter *t*, indicating its consistency across spatial scales of analysis. This separation places auditory and frontal regions at opposite ends of the auditory processing hierarchy, linked by ventral and dorsal processing streams[12-14]. Finally, PFC and sensorimotor ROIs form tight clusters on the periphery of embedding space, consistent with the respective executive and action functions these groups of ROIs subserve.

Network hubs

This study identified a number of ROIs characterized by central location within embedding space and mean connectivity. One of such ROIs, PCC/preCun, is well-established as a global hub based on analysis of RS functional connectivity derived from fMRI[35]. More relevant to the organization auditory cortical networks are the hubs identified in the temporal lobe. Previous studies have attributed to the anterior temporal lobe a central role in semantic processing and social memory[32, 70, 82]. This region has been envisioned to serve as a global transmodal hub, responsible for transformation from sensory domain-specific to domain-general representations[32, 83, 84]. The present iEEG results identified "global hub" ROIs in parts of the anterior temporal lobe (STGA, MTGA, ITGA). Additionally, MTGM and STSL were characterized by high mean connectivity and central position within embedding space. Although patients with semantic dementia have ATL degeneration[85, 86], the damage is often more widespread[87] and can include more caudal portions of MTG and ITG. The global hub-like connectivity profile of STSL suggests that this area also contributes to integration of information from multiple modalities, and is consistent with the diverse array of functions attributed to the STS based on previous neuroimaging studies (reviewed in[64, 88]).

Surprisingly, TP did not exhibit connectivity properties consistent with a global hub role, unlike other ATL structures. TP was more closely associated in embedding space with limbic structures. This suggests a more central role for TP in mediating interactions between multimodal integration centers in the ATL and structures subserving memory functions. The heterogeneity of ATL ROIs in terms of their global hub-like connectivity profiles is consistent with the observation that that the terminal fields of white matter tracts converging in the ATL only partially overlap[32, 89, 90]).

Hemispheric lateralization

Although speech and language networks are classically described as highly lateralized, imaging studies have demonstrated widespread and bilateral activation of auditory ROIs during speech and language tasks[91-93]. This study found no evidence for hemispheric differences in cortical

572 functional organization when all sampled brain regions were included in the analysis.
573 Furthermore, no differences were found when the comparison was restricted to speech and
574 language ROIs in the language dominant versus non-dominant hemispheres (Figure 6). The
575 present results are consistent with the fMRI study of Jackson et al.[30] that demonstrated similar
576 RS connectivity patterns between left and right temporal lobe (but see[8]). Thus, neither
577 anatomical nor task-specific functional hemispheric asymmetries necessarily translate into
578 distinct functional geometry configurations between the language dominant and non-dominant
579 hemisphere. While the present data suggest that at least during RS, the organization of these
580 networks is not hemisphere-specific, it is possible, that this organization changes during the
581 processing of auditory stimuli.

582

583 *Caveats & limitations*

584 A key concern regarding all human iEEG studies is that the study participants may not be
585 representative of a healthy population. With regards to the present study, consistent results
586 were observed across subjects despite differences in seizure disorder histories, antiepileptic
587 medication regimens, and the location of seizure foci. Importantly, the findings of the present
588 study are comparable to results obtained previously in healthy subjects using fMRI[35].

589 Another caveat is that our iEEG dataset, however extensive, did not sample the entire brain,
590 and it was not possible to infer connectivity with regions that were not sampled. To address
591 this, we used DME analysis of functional connectivity derived from fMRI data to establish that
592 the organization of ROIs in embedding space was robust to the exclusion of unsampled cortical
593 ROIs. Although there was a greater effect of sparse, non-uniform sampling within an ROI, there
594 was still considerable similarity in functional organization to embeddings derived from averages
595 across the entire ROI.

596 Importantly, subcortical structures, such as the thalamus, that link sensory and higher order
597 networks[94], were not sampled in these subjects. The functional organization presented here is
598 likely influenced indirectly by the multiple thalamo-cortical pathways carrying lemniscal and
599 extralemniscal sensory information to cortex[62, 95]. Although previous fMRI studies of RS
600 networks focused exclusively on cortical ROIs and did not consider the role of the thalamus and
601 other subcortical structures, these studies have yielded valuable insights into the functional
602 organization of the human cortical networks[96, 97].

603

604 *Concluding remarks and future directions*

605 The present study extends the DME analysis approach to characterize and visualize functional
606 relationships between cortical regions investigated using iEEG recordings. Using this approach,
607 we have contributed to the resolution of several outstanding issues regarding the functional
608 organization of human auditory cortical networks. This approach can advance our

understanding of changes in brain organization underlying transitions in states of arousal in sleep and anesthesia, disorders of consciousness, as well as reorganization of cortical functional geometry secondary to lesions. These results lay the foundation for future work that will investigate the organization of these networks during active speech and language processing.

613 **Online Methods**

614 *Subjects*

615 The study was carried out in 46 neurosurgical patients (20 females) diagnosed with medically
616 refractory epilepsy who were undergoing chronic invasive electrophysiological monitoring to
617 identify seizure foci prior to resection surgery (Supplementary Table 1). Research protocols
618 were approved by the University of Iowa Institutional Review Board and the National Institutes
619 of Health, and written informed consent was obtained from all subjects. Research participation
620 did not interfere with acquisition of clinically necessary data, and subjects could rescind
621 consent for research without interrupting their clinical management.

622 All subjects except two were native English speakers. The subjects were predominantly right-
623 handed (39 out of 46); six subjects were left-handed, and one had bilateral handedness. The
624 majority of subjects (32 out of 46) were left language-dominant, as determined by Wada test.
625 Two subjects were right hemisphere-dominant; and one had bilateral language dominance. The
626 remaining 11 subjects were not evaluated for language dominance; 9 of them were right-
627 handed and thus were assumed left language-dominant for the purposes of the analysis of
628 lateralization (see below). The remaining two subjects who did not undergo Wada test and who
629 were left-handed were not included in that analysis.

630 All subjects underwent audiological and neuropsychological assessment prior to electrode
631 implantation, and none had auditory or cognitive deficits that would impact the results of this
632 study. The subjects were tapered off their antiepileptic drugs during chronic monitoring when
633 RS data were collected.

634

635 *Experimental procedures*

636 *Pre-Implantation neuroimaging.* All subjects underwent whole-brain high-resolution T1-
637 weighted structural MRI scans before electrode implantation. In a subset of ten subjects
638 (Supplementary Table 2), RS functional MRI (RS-fMRI) data were collected as well and used for
639 estimates of functional connectivity. The scanner was a 3T GE Discovery MR750W with a 32-
640 channel head coil. The pre-electrode implantation anatomical T1 scan (3D FSPGR BRAVO
641 sequence) was obtained with following parameters: FOV = 25.6 cm, flip angle = 12 deg., TR =
642 8.50 ms, TE = 3.29 ms, inversion time = 450 ms, voxel size = 1.0 × 1.0 × 0.8 mm. For RS-fMRI, 5
643 blocks of 5-minute gradient-echo EPI runs (650 volumes) were collected with the following
644 parameters: FOV = 22.0 cm, TR = 2260 ms, TE = 30 ms, flip angle = 80 deg., voxel size = 3.45 x
645 3.45 x 4.0 mm. In some cases, fewer RS acquisition sequences were used in the final analysis
646 due to movement artifact or the full scanning session was not completed. For each subject, RS-
647 fMRI runs were acquired in the same session but non-contiguously (dispersed within an imaging
648 session to avoid habituation). Participants were asked to keep their eyes open, and a fixation
649 cross was presented through a projector.

650 *iEEG recordings.* iEEG recordings were obtained using either subdural and depth electrodes, or
651 depth electrodes alone, based on clinical indications. Electrode arrays were manufactured by
652 Ad-Tech Medical (Racine, WI). Subdural arrays, implanted in 36 subjects out of 46, consisted of
653 platinum-iridium discs (2.3 mm diameter, 5-10 mm inter-electrode distance), embedded in a
654 silicon membrane. Stereotactically implanted depth arrays included between 4 and 12
655 cylindrical contacts along the electrode shaft, with, 5-10 mm inter-electrode distance. A
656 subgaleal electrode, placed over the cranial vertex near midline, was used as a reference in all
657 subjects. All electrodes were placed solely on the basis of clinical requirements, as determined
658 by the team of epileptologists and neurosurgeons (Nourski and Howard, 2015).

659 No-task RS data were recorded in the dedicated, electrically shielded suite in The University of
660 Iowa Clinical Research Unit while the subjects lay in the hospital bed. RS data were collected 6.4
661 +/- 3.5 days (mean ± SD; range 1.5 – 20.9) after electrode implantation surgery. In the first 15
662 subjects (L275 through L362), data were recorded using a TDT RZ2 real-time processor (Tucker-
663 Davis Technologies, Alachua, FL). In the remaining 31 subjects (R369 through L585), data
664 acquisition was performed using a Neuralynx Atlas System (Neuralynx Inc., Bozeman, MT).
665 Recorded data were amplified, filtered (0.1–500 Hz bandpass, 5 dB/octave rolloff for TDT-
666 recorded data; 0.7–800 Hz bandpass, 12 dB/octave rolloff for Neuralynx-recorded data) and
667 digitized at a sampling rate of 2034.5 Hz (TDT) or 2000 Hz (Neuralynx). The durations of
668 recordings were 13 +/- 11 min. In all but two subjects, recording durations were between 10
669 and 22 mins.; in one subject duration was 6 min., and in one subject the duration was 81 min.

670

671 *Data analysis*

672 *Anatomical reconstruction and ROI parcellation.* Localization of recording sites and their
673 assignment to ROIs relied on post-implantation T1-weighted anatomical MRI and post-
674 implantation computed tomography (CT). All images were initially aligned with pre-operative T1
675 images using linear coregistration implemented in FSL (FLIRT)[98]. Electrodes were identified in
676 the post-implantation MRI as magnetic susceptibility artifacts and in the CT as metallic
677 hyperdensities. Electrode locations were further refined within the space of the pre-operative
678 MRI using three-dimensional non-linear thin-plate spline warping[99], which corrected for post-
679 operative brain shift and distortion. The warping was constrained with 50-100 control points,
680 manually selected throughout the brain, which were visually aligned to landmarks in the pre-
681 and post-implantation MRIs.

682 To pool data across subjects, the dimensionality of connectivity matrices was reduced by
683 assigning electrodes to one of 58 ROIs organized into 6 ROI groups (see Fig. 1; Supplementary
684 Table 2) based upon anatomical reconstructions of electrode locations in each subject. For
685 subdural arrays, it was informed by automated parcellation of cortical gyri[100, 101] as
686 implemented in the FreeSurfer software package. For depth arrays, ROI assignment was
687 informed by MRI sections along sagittal, coronal, and axial planes. For recording sites in

688 Heschl's gyrus (HG), delineation of the border between core auditory cortex adjacent non-core
689 areas (posteromedial and anterolateral HG; HGPM and HGAL, respectively) was performed in
690 each subject using physiological criteria[102, 103]. Specifically, recording sites were assigned to
691 HGPM if they exhibited phase-locked (frequency-following) responses to 100 Hz click trains and
692 if the averaged evoked potentials to these stimuli featured short-latency (<20 ms) peaks. Such
693 response features are characteristic for HGPM and are not present within HGAL (Brugge et al.,
694 2009). Additionally, correlation coefficients between average evoked potential waveforms
695 recorded from adjacent sites were examined to identify discontinuities in response profiles
696 along HG that could be interpreted as reflecting a transition from HGPM to HGAL. Superior
697 temporal gyrus (STG) was subdivided into posterior and middle non-core auditory cortex ROIs
698 (STGP and STGM), and auditory-related anterior ROI (STGA) using the transverse temporal
699 sulcus and ascending ramus of the Sylvian fissure as macroanatomical boundaries. The insula
700 was subdivided into posterior and anterior ROIs, with the former considered within the
701 auditory-related ROI group[7]. Middle and inferior temporal gyrus (MTG and ITG) were each
702 divided into posterior, middle, and anterior ROIs by diving the gyrus into three approximately
703 equal-length thirds. Angular gyrus (AG) was divided into posterior and anterior ROIs (AGP and
704 AGA) using the angular sulcus as a macroanatomical boundary. Anterior cingulate cortex was
705 identified by automatic parcellation in FreeSurfer and was considered as part of the prefrontal
706 ROI group, separately from the rest of the cingulate gyrus. Postcentral and precentral gyri were
707 each divided into ventral and dorsal portions using the y_{MNI} coordinate (see below) of 40 mm as
708 a boundary. Recording sites identified as seizure foci or characterized by excessive noise, and
709 depth electrode contacts localized to the white matter or outside brain, were excluded from
710 analyses and are not listed in Supplementary Table 2.

711 *Preprocessing of fMRI data.* Standard preprocessing was applied to the RS-fMRI data acquired
712 in the pre-implantation scan using FSL's FEAT pipeline, including de-spiking and slice timing
713 correction, and spatial alignment. White matter and ventricles were masked using Freesurfer
714 parcellation. Nuisance regressors, including the global signal, were extracted from these masks
715 and detrended with second order polynomials. Temporal bandpass filtering was 0.008–0.08 Hz.
716 Regression was performed using the time series calculated above as well as motion parameters
717 and their derivatives. Spatial smoothing was applied with a 6 mm full-width at half maximum
718 Gaussian kernel. The first two images from each run were discarded. Frame censoring was
719 applied when the Euclidean norm of derivatives of motion parameters exceeded 0.3 mm[104]. All
720 runs were processed in native EPI space, then the residual data was transformed to MNI152
721 and the data was concatenated.

722 *Preprocessing of iEEG data*. Analysis of iEEG data was performed using custom software
723 written in MATLAB Version 2020a programming environment (MathWorks, Natick, MA, USA).
724 After initial rejection of recording sites identified as seizure foci, several automated steps were
725 taken to exclude recording channels and time intervals contaminated by noise. First, channels
726 were excluded if average power in any frequency band (broadband, delta, theta, alpha, beta,
727 gamma, or high gamma) exceeded 3.5 standard deviations of the average power across all

728 channels for that subject. Next, transient artifacts were detected by identifying voltage
729 deflections exceeding 10 standard deviations on a given channel. A time window was identified
730 extending before and after the detected artifact until the voltage returned to the zero-mean
731 baseline plus an additional 100 ms buffer before and after. High-frequency artifacts were also
732 removed by masking segments of data with high gamma power exceeding 5 standard
733 deviations of the mean across all segments. Only time bins free of these artifact masks were
734 considered in subsequent analyses. Artifact rejection was applied across all channels
735 simultaneously so that all connectivity measures are derived from the same time windows.
736 Occasionally, particular channels survived the initial average power criteria yet had frequent
737 artifacts that led to loss of data across all the other channels. There is a tradeoff in rejecting
738 artifacts (losing time across all channels) and rejecting channels (losing all data for that
739 channel). If artifacts occur on many channels, there is little benefit to excluding any one
740 channel; however, if frequent artifacts occur on one or simultaneously on up to a few channels,
741 omitting these can save more data from other channels than those channels contribute at all
742 other times. We chose to optimize the total data retained, channels × time windows, and
743 omitted some channels when necessary. To remove shared signals unlikely to derive from brain
744 activity, data from good channels were high-pass filtered above 200 Hz and a spatial filter
745 derived from the singular value decomposition omitting the first singular vector. This spatial
746 filter was then applied to the broadband signal to remove this common signal.

747 *Connectivity analysis.* For RS-fMRI data, BOLD signals were averaged across voxel groupings and
748 functional connectivity calculated as Pearson correlation coefficients. Voxel groupings were
749 either based on the Schaefer-Yeo 400 parcellation scheme[54] in MNI-152 space, or were based
750 on iEEG electrode location in subject space. For the latter, fMRI voxels were chosen to
751 represent comparable regions of the brain recorded by iEEG electrodes. For each electrode, the
752 anatomical coordinates of the recording site were mapped to the closest valid MRI voxel, *E*, and
753 a sphere of 25 voxels (25 mm^3) centered on *E* used as the corresponding recording site. This
754 process was repeated for all *N* electrodes in the same ROI, and a single time series computed as
755 the average of the fMRI BOLD signal in these *N*×25 voxels. These averages were used to
756 compute an ROI-by-ROI connectivity matrix for RS-fMRI data. For comparisons between iEEG
757 and fMRI embeddings, voxels were processed in subject space and ROI labels from the
758 parcellation scheme illustrated in Figure 1 and Supplementary Table 2 were applied to the fMRI
759 data. For comparisons between fMRI embeddings derived from all cortical ROIs versus fMRI
760 embeddings derived from just ROIs sampled in the iEEG experiments, electrode locations were
761 transformed from subject space to MNI-152 space, then assigned to ROIs within the Schaefer-
762 Yeo 400 scheme.

763 For iEEG data, two measures of functional (non-directed) connectivity were used: the debiased
764 weighted phase lag index (wPLI;[105]), a measure of phase synchronization, and the
765 orthogonalized band power envelope correlation[36]. Both measures avoid artifacts due to
766 volume conduction by discounting connectivity near zero phase lag. For both measures, data

767 were divided into 60-second segments, pairwise connectivity estimated in each segment, and
768 then connectivity estimates averaged across all segments for that subject.

769 wPLI was estimated for each data segment and every recording site pair from the sign of the
770 imaginary part of the cross-spectrum at each frequency and averaged across frequencies within
771 each band of interest (theta: 4-8 Hz, alpha: 8-13 Hz, beta: 13-30 Hz). The cross spectrum was
772 calculated from the demodulated band transform (DBT)[106] as described previously[107].

773 Envelope correlations were estimated for each data segment and every recording site as in[36],
774 except time-frequency decomposition was performed using the DBT rather than wavelets. For
775 each frequency band (theta: 4-8 Hz, alpha: 8-13 Hz, beta: 13-30 Hz, gamma: 30-70 Hz; high
776 gamma: 70-120 Hz), the power at each time bin was calculated as the average (across
777 frequencies) log of the squared amplitude. For each pair of signals *X* and *Y*, one was
778 orthogonalized to the other by taking the magnitude of the imaginary component of the
779 product of one signal with the normalized complex conjugate of the other:

780 $$Y_{orth} = |\mathrm{Im}\{Y \times X^{*}/|X|\}|$$

781 Both signals were band-pass filtered (0.2 – 1 Hz), and the Pearson correlation calculated
782 between signals. The process was repeated by orthogonalizing in the other direction and the
783 overall envelope correlation for a pair of recording sites was the average of the two Pearson
784 correlations.

785 Prior to diffusion map embedding, connectivity matrices were thresholded by saving at least
786 the top third (rounded up) connections for every row, as well as their corresponding columns
787 (to preserve symmetry). We also included any connections making up the minimum spanning
788 tree of the graph represented by the elementwise reciprocal of the connectivity matrix to
789 ensure the graph is connected.

790 *ROI-based connectivity analysis.* Connectivity between ROIs was computed as the average
791 envelope correlation or wPLI value between all pairs of recording sites in the two ROIs. For
792 analyses in which connectivity was summarized across subjects (Fig. 3-9), we used only a subset
793 of ROIs such that every possible pair of included ROIs was represented in at least two subjects
794 (Supplementary Table 2). This list of ROIs was obtained by iteratively removing ROIs with the
795 worst cross-coverage with other ROIs until every ROI remaining had sufficient coverage with all
796 remaining ROIs.

797 *Diffusion map embedding*. See the Appendix for details about DME. In brief, the connectivity
798 matrix **K =** [*k*(*i*,*j*)] is normalized by degree to yield a transition probability matrix **P**. DME consists
799 of performing an eigendecomposition of **P**, with eigenvalues scaled according to the free
800 parameter *t*, which sets the spatial scale of the analysis. If the recording sites are
801 conceptualized as nodes on a graph with edges defined by **K**, then **P** can be understood as the
802 transition probability matrix for a 'random walk' or a 'diffusion' on the graph (see Appendix;[33,
803 34]). The parameter *t* is the number of time steps in that random walk; larger values of *t*

correspond to exploring the structure of the data at larger spatial scales. In the analyses presented here, $k(i,j)$ is either the orthogonalized power envelope correlations, or the debiased weighted phase lag index. We note that in recent applications of DME to fMRI functional connectivity data, a **K** was first transformed by applying cosine similarity[35]. However, this additional step has not been universally implemented (e.g.,[108], nor is it required within the mathematical framework of DME[33, 34]. In the case of the dataset presented here, applying cosine similarity to the data served to smear the data in embedding space, increasing variance, and decreasing separation between ROIs, but otherwise produced qualitatively similar results.

In two sets of analyses presented here, pairs of embeddings were compared to each other: in the analysis of lateralization of speech and language networks, and in the comparison between iEEG and fMRI data. To do that, we used a change of basis operator to map embeddings into a common embedding space using the method described in Coifman et al 2014[34].

Dimensionality reduction – low rank approximations to **P**. Diffusion map embedding offers an opportunity to reduce the dimensionality of the underlying data by considering only those dimensions that contribute importantly to the structure of the data, as manifested in the structure of the transition probability matrix **P**. We used the eigenvalue spectrum of **P** to determine its ideal low rank approximation, balancing dimensionality reduction and information loss. Because **P** is real and symmetric, the magnitude of the eigenvalues is identical to the singular values of **P**. The singular values tell us about the fidelity of low rank approximations to **P**. Specifically, if **P** has a set of singular values $\sigma_1 \geq \sigma_1 \geq \ldots \geq \sigma_n$, then for any integer $k \geq 1$,

$$\min_{\widetilde{\mathbf{P}_k}} \left\| \mathbf{P} - \widetilde{\mathbf{P}_k} \right\|_2 = \sigma_{k+1},$$

where $\widetilde{\mathbf{P}_k}$ is the rank-k approximation to **P**. Thus, the magnitude of the eigenvalues corresponds to the fidelity of the lower dimensional approximation, and the difference in the magnitude of successive eigenvalues represents the improvement in that approximation as the dimensionality increases. The spectrum of **P** invariably have an inflection point ("elbow"), separating two sets of eigenvalues λ_i: those whose magnitude decreases more quickly with increasing i, and those beyond the inflection point whose magnitude decreases more slowly with increasing i. The inflection point thus delineates the number of dimensions that are most important for approximating **P**. The inflection point k_{infl} was identified algorithmically[109], and the number of dimensions retained set equal to $k_{\text{infl}} - 1$.

Comparing distances in embedding space. The relative distance between points in an embedding provides insight into the underlying functional geometry. In several analyses presented here, two embeddings of identical sets of ROIs were compared as ROI distances within the two embeddings. After mapping to a common space and reducing dimensionality as described above, the two embeddings A and B were used to create the pairwise distance matrices A` and B`. The correlation between the upper triangles (excluding the diagonal) of the corresponding elements in the distance matrices was then computed.

842 *Signal to noise (SNR) characteristics.* To measure the robustness of the embedding analysis to
843 variability over time, an SNR was computed as follows. For each subject, a channel × channel **P**
844 matrix was calculated for each 60 s segment of data. For each segment, DME analysis was
845 applied and a channel × channel distance matrix calculated. These distance matrices were
846 averaged across segments. The 'signal' of interest was defined as the variability (standard
847 deviation) of this averaged distance matrix (ignoring the diagonals). The 'noise' was defined as
848 the variability across time, estimated for each element of the distance matrix as the standard
849 deviation across segments, then averaged across the elements of the matrix. The SNR for
850 functional connectivity itself was computed in an analogous manner, using the original channel
851 × channel connectivity matrix rather than the matrix of embedding distances.

852 *Estimating precision in position and distances in embedding space.* To obtain error estimates for
853 both ROI locations in embedding space and embedding distance between ROIs, average ROI by
854 ROI adjacency matrices were calculated. This was done by drawing each edge from an averaged
855 bootstrap sample across subjects, obtaining 10,000 such adjacency matrices, and performing
856 diffusion map embedding for each. For locations in embedding space, these embeddings were
857 then mapped via the change of basis procedure described above to the original group average
858 embedding space. For each ROI, the mapped bootstrap iterations produced a cloud of locations
859 in embedding space which were summarized by the standard deviation in each dimension. For
860 embedding distances, no change of basis was necessary because distances were preserved
861 across bases.

862 To compare the positions of STSL versus STSU relative to canonical auditory cortical ROIs
863 (HGPM, HGAL, PT, PP, STGP, and STGM) or ROIs involved in semantic processing (STGA, MTGA,
864 MTGP, ITGA, ITGP, TP, AGA, AGP, SMG, IFGop, IFGtr, IFGor[32, 42-44]), we calculated the average
865 pairwise distance from STSL or STSU to each such ROI. The difference between these averages
866 was compared to a null distribution obtained by Monte Carlo sampling of the equivalent
867 statistic obtained by randomly exchanging STSL/STSU labels by subject. The specific
868 comparisons performed were chosen *a priori* to constrain the number of possible hypotheses
869 to test; pairwise comparisons of all possible ROI pairs (let alone comparisons of all higher-order
870 groupings) would not have had sufficient statistical power under appropriate corrections for
871 multiple comparisons. Though different choices could have been made for inclusion in the
872 "semantic processing" category, exchanging one or two of these ROIs would not strongly
873 influence the average distance in a group of twelve ROIs.

874 *Hierarchical clustering.* Agglomerative hierarchical clustering was done using the *linkage*
875 function in MATLAB, with Euclidean distance as the distance metric and Ward's linkage
876 (minimum variance algorithm) as the linkage method. The ordering of ROIs along the horizontal
877 axis in the dendrogram was determined using the *optimalleaforder* function in MATLAB, with
878 the optimization criterion set to 'group'.

879 *Comparing language dominant/non-dominant hemispheres.* To test for differences in
880 embedding location between language dominant and non-dominant hemispheres, two

881 measures were considered: different location of individual ROIs in embedding space, and
882 different pairwise distances between ROIs in embedding space. To calculate differences in
883 location of individual ROIs, dominant/non-dominant average embeddings were mapped to a
884 common space (from an embedding using the average across all subjects regardless of language
885 dominance) using the change of basis operator. The language-dominant location difference for
886 a specific ROI was calculated as the Euclidean distance between the two locations of each ROI
887 in this common space. For pairwise distances, the change of basis is irrelevant, so pairwise
888 Euclidean distances were calculated in embedding space for each hemisphere and then
889 subtracted to obtain a difference matrix. To determine whether the differences in location or
890 pairwise distances were larger than expected by change, random permutations of the
891 dominant/non-dominant labels were used to generate empirical null distributions. Since a p-
892 value was obtained for every pair of electrodes, multiple comparisons were corrected using
893 FDR.

894

895 *Analyses of fMRI connectivity in embedding space.* Two sets of analyses were performed using
896 fMRI data. First, iEEG and fMRI data were compared in embedding space. In this analysis,
897 connectivity based on RS-fMRI data from voxels located at electrode recording sites was
898 compare with the corresponding connectivity matrix derived from iEEG data. The embedding
899 analysis was applied to the two connectivity matrices, all pairwise inter-ROI distances
900 computed, and iEEG and fMRI data compared using the correlation of the pairwise ROI
901 distances. The second analysis was to compare embeddings derived from all ROIs in the RS-
902 fMRI scans to those derived from just ROIs sampled with iEEG electrodes. Here, ROI×ROI
903 connectivity matrices were computed for all ROIs, then embeddings created from the full
904 matrices or from matrices containing just rows and columns corresponding to the ROIs sampled
905 with iEEG.

Appendix: Diffusion Map Embedding

In the framework of DME, we consider a space X that is the set of N recording sites. We compute the similarity between those sites based on the time varying signals recorded at each site, defining similarity as the functional connectivity measure $k(x_i,x_j)$.

Define the matrix **K** whose i,j^{th} element is $k(x_i,x_j)$. $k(x_i,x_j)$ is required to be symmetric, i.e., $k(x_i,x_j) = k(x_j,x_i)$, and positivity preserving, i.e. $k(x_i,x_j) > 0$ for all $[i,j]$, to allow for spectral analysis of a normalized version of **K**.

From X and **K** we can construct a weighted graph Γ in which the vertices are the nodes and the edge weights are $k(x_i,x_j)$. We take random walks on the graph at time steps t = 1, 2, …, jumping from node x_i to node x_j at each time step, with the (stochastic) decision as to which node should be visited next depending on $k(x_i,x_j)$.

Define

$$p(x_i,x_j) = k(x_i,x_j)/d(x_i),$$

where

$$d(x_i) = \Sigma_j[k(x_i,x_j)]$$

is the degree of node x_i. Normalizing $k(x_i,x_j)$ in this way allows us to interpret it as the probability $p(x_i,x_j)$ that we'll jump from vertex x_i to vertex x_j in a single time step of our random walk.

If we consider a single time step, we only capture the structure in X on a very local scale, since we can only jump between vertices that are directly connected. As we run the random walk forward in time, we begin to explore more of our neighborhood, and we begin to explore other neighborhoods as well. Two vertices x_i and x_j that have similar connectivity to the rest of the network have a high probability of being connected during these longer walks because they are themselves are connected to similar groups of vertices, and so there are many possible paths between x_i and x_j.

The diffusion operator (matrix) $\mathbf{P} = [p(x_i,x_j)]$ describes how things diffuse from node to node in our graph. If **v** is a $N\times1$ vector (i.e., a value assigned to each vertex, for example representing an input to each node), then **P** describes what will happen to that input as time goes on.

$$\mathbf{Pv} = [p(x_1,x_1)\mathbf{v}[x_1]+p(x_1,x_2)\mathbf{v}[x_2]+\ldots;\ p(x_2,x_1)\mathbf{v}[x_1]+p(x_2,x_2)\mathbf{v}[x_2]+\ldots;\ldots]^T$$

If, for example, all the nodes were insular, with $p(x_i,x_i)=1$ for all i, and $p(x_i,x_j)=0$ otherwise, **Pv** = **v**, i.e., no diffusion occurs. If the probabilities are more distributed, **Pv** would tell you how much things diffuse out from each node given the starting condition of **v**. Importantly, $\mathbf{P}^k\mathbf{v}$ would tell you what that distribution looks like after k time steps.

The eigenvector expansion of **P** based on its eigenvectors ψ_j and eigenvalues , λ_j, j = 1...N, is a natural method for uncovering structure in **P** because each eigenvector of **P** is a dimension along which interesting organizational features emerge. That is, clusters of related points (communities) tend to be distinct and ordered along these dimensions. In fact, we could preserve a lot of information about **P** if we kept just a subset of M of these vectors and forgot about the rest. The information we want to preserve in the context of diffusion map embedding is the functional distance between the data at two nodes given t time steps to meander through the graph. We can define the diffusion map

$$\Psi^{(t)}(x_i) = [\lambda_1{}^t\psi_1(x_i), \lambda_1{}^t\psi_1(x_i), \ldots, \lambda_M{}^t\psi_M(x_i)]^T,$$

which maps each point x in X to a point in an embedding space of dimension $M \leq$ N. In this space, the diffusion distance D, which is the Euclidean distance between points, is the difference in the probability distributions linking x_i to the rest of the network and x_j to the rest of the network:

$$D^{(t)}(x_i,x_j)^2 = ||\Psi^{(t)}(x_i) - \Psi^{(t)}(x_j)||_{l2}.= ||p^{(t)}(x_i,:)- p^{(t)}(x_j,:)||^2{}_{l2}.$$

We return now to the parameter t, which corresponds to the time scale of the diffusion process (i.e., the number of steps in the random walk on the graph). As t progresses, the coordinates of the data in embedding space are scaled according to $\lambda_i{}^t$, where λ_i is the eigenvalue of the ith dimension being scaled. Thus, the value of t sets the spatial scale of the analysis. Because $|\lambda_i|<1\ \forall\ i$, at higher values of t each dimension will be scaled down ('collapse'), with the dimension corresponding to max($|\lambda_i|$) (i.e., λ_1) scaled the least.

It's often the case that we make repeated measurements under different experimental conditions, and we would like to compare our brain data recorded under these different conditions. For example, we might make measurements in different subjects, or in different cohorts of subjects. We can use the DME framework to make those comparisons, but it takes some extra work. Consider two sets of data α and β, and the data spaces X_α and X_β. The problem is that X_α and X_β are different spaces with different kernels k_α and k_β. This means that the eigenvectors for $\mathbf{P}_\alpha$ and $\mathbf{P}_\beta$ will be different, and data projected into a space defined by some subset of the eigenvectors cannot be compared directly. The solution is to apply a change of basis operator to one set of the eigenvectors to get the data into the same embedding space[34]:

$$D^{(t)}(x_{i|\alpha},x_{i|\beta}) = ||\Psi^{(t)}{}_\alpha(x) - O_{\beta\rightarrow\alpha}\Psi^{(t)}{}_\beta(x)||_{l2}.$$

Where the change of basis operator $O_{\beta\rightarrow\alpha}$ is defined as

$$O_{\beta\rightarrow\alpha}\ \mathbf{v} = \Sigma_j[\mathbf{v}(j)<\psi^{(i)}{}_\alpha\ ,\psi^{(j)}{}_\beta>]_{i>=1},$$

Where <**a**,**b**> is the inner product of **a** and **b**.

REFERENCES CITED

1. Felleman, D.J. & Van Essen, D.C. Distributed hierarchical processing in the primate cerebral cortex. *Cereb.Cortex* **1**, 1-47 (1991).
2. Hochstein, S. & Ahissar, M. View from the top: hierarchies and reverse hierarchies in the visual system. *Neuron* **36**, 791-804 (2002).
3. Geschwind, N. The organization of language and the brain. *Science* **170**, 940-944 (1970).
4. Hagoort, P. The neurobiology of language beyond single-word processing. *Science* **366**, 55-58 (2019).
5. Friederici, A.D., Meyer, M. & von Cramon, D.Y. Auditory language comprehension: an event-related fMRI study on the processing of syntactic and lexical information. *Brain Lang* **75**, 289-300 (2000).
6. Angulo-Perkins, A.*, et al.* Music listening engages specific cortical regions within the temporal lobes: differences between musicians and non-musicians. *Cortex* **59**, 126-137 (2014).
7. Zhang, Y.*, et al.* The Roles of Subdivisions of Human Insula in Emotion Perception and Auditory Processing. *Cereb Cortex* **29**, 517-528 (2019).
8. Abrams, D.A., Kochalka, J., Bhide, S., Ryali, S. & Menon, V. Intrinsic functional architecture of the human speech processing network. *Cortex* **129**, 41-56 (2020).
9. Nourski, K.V.*, et al.* Electrophysiology of the Human Superior Temporal Sulcus during Speech Processing. *Cereb Cortex* **31**, 1131-1148 (2021).
10. Ungerleider, L.G. & Mishkin, M. Two visual systems. in *Analysis of visual behavior* (ed. D.J. Ingle, M.A. Goodale & R.J.W. Mansfield) 549-586 (MIT Press, Cambridge, MA, 1982).
11. Goodale, M.A. & Milner, A.D. Separate visual pathways for perception and action. *Trends Neurosci* **15**, 20-25 (1992).
12. Rauschecker, J.P. & Scott, S.K. Maps and streams in the auditory cortex: nonhuman primates illuminate human speech processing. *Nat Neurosci* **12**, 718-724 (2009).
13. Hickok, G. & Poeppel, D. The cortical organization of speech processing. *Nat Rev Neurosci* **8**, 393-402 (2007).
14. Friederici, A.D. The cortical language circuit: from auditory perception to sentence comprehension. *Trends Cogn Sci* **16**, 262-268 (2012).
15. Cloutman, L.L. Interaction between dorsal and ventral processing streams: where, when and how? *Brain Lang* **127**, 251-263 (2013).
16. Hickok, G. & Poeppel, D. Neural basis of speech perception. *Handb Clin Neurol* **129**, 149-160 (2015).
17. Rauschecker, J.P. Where, When, and How: Are they all sensorimotor? Towards a unified view of the dorsal pathway in vision and audition. *Cortex* **98**, 262-268 (2018).
18. Scott, S.K. The neurobiology of speech perception and production--can functional imaging tell us anything we did not already know? *J Commun Disord* **45**, 419-425 (2012).
19. Woods, D.L. & Alain, C. Functional imaging of human auditory cortex. *Curr Opin Otolaryngol Head Neck Surg* **17**, 407-411 (2009).
20. Munoz-Lopez, M.M., Mohedano-Moriano, A. & Insausti, R. Anatomical pathways for auditory memory in primates. *Front Neuroanat* **4**, 129 (2010).
21. Kraus, K.S. & Canlon, B. Neuronal connectivity and interactions between the auditory and limbic systems. Effects of noise and tinnitus. *Hear Res* **288**, 34-46 (2012).

1018 22. Husain, F.T. & Schmidt, S.A. Using resting state functional connectivity to unravel networks of
1019 tinnitus. *Hear Res* **307**, 153-162 (2014).
1020 23. Kumar, S.*, et al.* A Brain System for Auditory Working Memory. *J Neurosci* **36**, 4492-4505 (2016).
1021 24. Kumar, S.*, et al.* Oscillatory correlates of auditory working memory examined with human
1022 electrocorticography. *Neuropsychologia* **150**, 107691 (2021).
1023 25. McGettigan, C. & Scott, S.K. Cortical asymmetries in speech perception: what's wrong, what's
1024 right and what's left? *Trends Cogn Sci* **16**, 269-276 (2012).
1025 26. Turkeltaub, P.E. & Coslett, H.B. Localization of sublexical speech perception components. *Brain*
1026 *Lang* **114**, 1-15 (2010).
1027 27. Leaver, A.M. & Rauschecker, J.P. Cortical representation of natural complex sounds: effects of
1028 acoustic features and auditory object category. *J Neurosci* **30**, 7604-7612 (2010).
1029 28. Eisner, F., McGettigan, C., Faulkner, A., Rosen, S. & Scott, S.K. Inferior frontal gyrus activation
1030 predicts individual differences in perceptual learning of cochlear-implant simulations. *J Neurosci* **30**,
1031 7179-7186 (2010).
1032 29. Saur, D.*, et al.* Ventral and dorsal pathways for language. *Proc Natl Acad Sci U S A* **105**, 18035-
1033 18040 (2008).
1034 30. Jackson, R.L., Bajada, C.J., Rice, G.E., Cloutman, L.L. & Lambon Ralph, M.A. An emergent
1035 functional parcellation of the temporal cortex. *Neuroimage* **170**, 385-399 (2018).
1036 31. Visser, M., Jefferies, E. & Lambon Ralph, M.A. Semantic processing in the anterior temporal
1037 lobes: a meta-analysis of the functional neuroimaging literature. *J Cogn Neurosci* **22**, 1083-1094 (2010).
1038 32. Ralph, M.A., Jefferies, E., Patterson, K. & Rogers, T.T. The neural and computational bases of
1039 semantic cognition. *Nat Rev Neurosci* **18**, 42-55 (2017).
1040 33. Coifman, R.R.*, et al.* Geometric diffusions as a tool for harmonic analysis and structure definition
1041 of data: diffusion maps. *Proc Natl Acad Sci U S A* **102**, 7426-7431 (2005).
1042 34. Coifman, R.R. & Hirn, M.J. Diffusion maps for changing data. *Applied and Computational*
1043 *Harmonic Analysis* **36**, 79-107 (2014).
1044 35. Margulies, D.S.*, et al.* Situating the default-mode network along a principal gradient of
1045 macroscale cortical organization. *Proc Natl Acad Sci U S A* **113**, 12574-12579 (2016).
1046 36. Hipp, J.F., Hawellek, D.J., Corbetta, M., Siegel, M. & Engel, A.K. Large-scale cortical correlation
1047 structure of spontaneous oscillatory activity. *Nat Neurosci* **15**, 884-890 (2012).
1048 37. Jones, E.G., Coulter, J.D. & Hendry, S.H. Intracortical connectivity of architectonic fields in the
1049 somatic sensory, motor and parietal cortex of monkeys. *J Comp Neurol* **181**, 291-347 (1978).
1050 38. Morel, A., Garraghty, P.E. & Kaas, J.H. Tonotopic organization, architectonic fields, and
1051 connections of auditory cortex in macaque monkeys. *J Comp Neurol* **335**, 437-459 (1993).
1052 39. Kaas, J.H. & Hackett, T.A. Subdivisions of auditory cortex and processing streams in primates.
1053 *Proc Natl Acad Sci USA* **97**, 11793-11799 (2000).
1054 40. Kaas, J.H. & Hackett, T.A. Subdivisions of auditory cortex and levels of processing in primates.
1055 *Audiol Neurootol* **3**, 73-85 (1998).
1056 41. Cavada, C., Company, T., Tejedor, J., Cruz-Rizzolo, R.J. & Reinoso-Suarez, F. The anatomical
1057 connections of the macaque monkey orbitofrontal cortex. A review. *Cereb Cortex* **10**, 220-242 (2000).
1058 42. Binder, J.R., Desai, R.H., Graves, W.W. & Conant, L.L. Where is the semantic system? A critical
1059 review and meta-analysis of 120 functional neuroimaging studies. *Cereb Cortex* **19**, 2767-2796 (2009).
1060 43. Humphreys, G.F., Hoffman, P., Visser, M., Binney, R.J. & Lambon Ralph, M.A. Establishing task-
1061 and modality-dependent dissociations between the semantic and default mode networks. *Proc Natl*
1062 *Acad Sci U S A* **112**, 7857-7862 (2015).
1063 44. Jackson, R.L., Hoffman, P., Pobric, G. & Lambon Ralph, M.A. The Semantic Network at Work and
1064 Rest: Differential Connectivity of Anterior Temporal Lobe Subregions. *J Neurosci* **36**, 1490-1501 (2016).

45. Remedios, R., Logothetis, N.K. & Kayser, C. An auditory region in the primate insular cortex responding preferentially to vocal communication sounds. *J Neurosci* **29**, 1034-1045 (2009).
46. Craig, A.D. Interoception: the sense of the physiological condition of the body. *Curr Opin Neurobiol* **13**, 500-505 (2003).
47. Kuehn, E., Mueller, K., Lohmann, G. & Schuetz-Bosbach, S. Interoceptive awareness changes the posterior insula functional connectivity profile. *Brain Struct Funct* **221**, 1555-1571 (2016).
48. Bernstein, L.E. & Liebenthal, E. Neural pathways for visual speech perception. *Front Neurosci* **8**, 386 (2014).
49. Knecht, S.*, et al.* Handedness and hemispheric language dominance in healthy humans. *Brain* **123 Pt 12**, 2512-2518 (2000).
50. Price, C.J. A review and synthesis of the first 20 years of PET and fMRI studies of heard speech, spoken language and reading. *Neuroimage* **62**, 816-847 (2012).
51. Schirmer, A., Fox, P.M. & Grandjean, D. On the spatial organization of sound processing in the human temporal lobe: a meta-analysis. *Neuroimage* **63**, 137-147 (2012).
52. Chang, E.F., Raygor, K.P. & Berger, M.S. Contemporary model of language organization: an overview for neurosurgeons. *J Neurosurg* **122**, 250-261 (2015).
53. Ardila, A., Bernal, B. & Rosselli, M. How Localized are Language Brain Areas? A Review of Brodmann Areas Involvement in Oral Language. *Arch Clin Neuropsychol* **31**, 112-122 (2016).
54. Schaefer, A.*, et al.* Local-Global Parcellation of the Human Cerebral Cortex from Intrinsic Functional Connectivity MRI. *Cereb Cortex* **28**, 3095-3114 (2018).
55. Hackett, T.A., Preuss, T.M. & Kaas, J.H. Architectonic identification of the core region in auditory cortex of macaques, chimpanzees, and humans. *J Comp Neurol.* **441**, 197-222 (2001).
56. Hackett, T.A. Anatomic organization of the auditory cortex. *Handb Clin Neurol* **129**, 27-53 (2015).
57. Woods, D.L.*, et al.* Functional properties of human auditory cortical fields. *Front Syst Neurosci* **4**, 155 (2010).
58. Barton, B., Venezia, J.H., Saberi, K., Hickok, G. & Brewer, A.A. Orthogonal acoustic dimensions define auditory field maps in human cortex. *Proc Natl Acad Sci U S A* **109**, 20738-20743 (2012).
59. Moerel, M., De Martino, F. & Formisano, E. An anatomical and functional topography of human auditory cortical areas. *Front Neurosci* **8**, 225 (2014).
60. Howard, M.A.*, et al.* Auditory cortex on the human posterior superior temporal gyrus. *J Comp Neurol.* **416**, 79-92 (2000).
61. Nourski, K.V.*, et al.* Spectral organization of the human lateral superior temporal gyrus revealed by intracranial recordings. *Cereb Cortex* **24**, 340-352 (2014).
62. Hamilton, L.S., Oganian, Y., Hall, J. & Chang, E.F. Parallel and distributed encoding of speech across human auditory cortex. *Cell* **184**, 4626-4639 e4613 (2021).
63. Hickok, G. The functional neuroanatomy of language. *Phys Life Rev* **6**, 121-143 (2009).
64. Beauchamp, M.S. The social mysteries of the superior temporal sulcus. *Trends Cogn Sci* **19**, 489-490 (2015).
65. Venezia, J.H.*, et al.* Auditory, Visual and Audiovisual Speech Processing Streams in Superior Temporal Sulcus. *Front Hum Neurosci* **11**, 174 (2017).
66. Zachlod, D.*, et al.* Four new cytoarchitectonic areas surrounding the primary and early auditory cortex in human brains. *Cortex* **128**, 1-21 (2020).
67. Belin, P., Zatorre, R.J., Lafaille, P., Ahad, P. & Pike, B. Voice-selective areas in human auditory cortex. *Nature* **403**, 309-312 (2000).
68. Deen, B., Koldewyn, K., Kanwisher, N. & Saxe, R. Functional Organization of Social Perception and Cognition in the Superior Temporal Sulcus. *Cereb Cortex* **25**, 4596-4609 (2015).
69. Wilson, S.M., Bautista, A. & McCarron, A. Convergence of spoken and written language processing in the superior temporal sulcus. *Neuroimage* **171**, 62-74 (2018).

1113 70. Olson, I.R., McCoy, D., Klobusicky, E. & Ross, L.A. Social cognition and the anterior temporal
1114 lobes: a review and theoretical framework. *Soc Cogn Affect Neurosci* **8**, 123-133 (2013).
1115 71. Fruhholz, S., Trost, W. & Kotz, S.A. The sound of emotions-Towards a unifying neural network
1116 perspective of affective sound processing. *Neurosci Biobehav Rev* **68**, 96-110 (2016).
1117 72. Mesulam, M.M. Paralimbic (mesocortical) areas. in *Principles of behavioral and cognitive*
1118 *neurology* 49-54 (Oxford University Press, New York, NY, 2000).
1119 73. Chanes, L. & Barrett, L.F. Redefining the Role of Limbic Areas in Cortical Processing. *Trends Cogn*
1120 *Sci* **20**, 96-106 (2016).
1121 74. Maller, J.J*., et al.* Revealing the Hippocampal Connectome through Super-Resolution 1150-
1122 Direction Diffusion MRI. *Sci Rep* **9**, 2418 (2019).
1123 75. Munoz-Lopez, M., Insausti, R., Mohedano-Moriano, A., Mishkin, M. & Saunders, R.C. Anatomical
1124 pathways for auditory memory II: information from rostral superior temporal gyrus to dorsolateral
1125 temporal pole and medial temporal cortex. *Front Neurosci* **9**, 158 (2015).
1126 76. Kahn, I., Andrews-Hanna, J.R., Vincent, J.L., Snyder, A.Z. & Buckner, R.L. Distinct cortical anatomy
1127 linked to subregions of the medial temporal lobe revealed by intrinsic functional connectivity. *J*
1128 *Neurophysiol* **100**, 129-139 (2008).
1129 77. Wang, S.F., Ritchey, M., Libby, L.A. & Ranganath, C. Functional connectivity based parcellation of
1130 the human medial temporal lobe. *Neurobiol Learn Mem* **134 Pt A**, 123-134 (2016).
1131 78. Upadhyay, J*., et al.* Effective and structural connectivity in the human auditory cortex. *J Neurosci*
1132 **28**, 3341-3349 (2008).
1133 79. Rocchi, F*., et al.* Common fronto-temporal effective connectivity in humans and monkeys.
1134 *Neuron* **109**, 852-868 e858 (2021).
1135 80. Michelmann, S*., et al.* Moment-by-moment tracking of naturalistic learning and its underlying
1136 hippocampo-cortical interactions. *Nat Commun* **12**, 5394 (2021).
1137 81. Hickok, G. Computational neuroanatomy of speech production. *Nat Rev Neurosci* **13**, 135-145
1138 (2012).
1139 82. Patterson, K., Nestor, P.J. & Rogers, T.T. Where do you know what you know? The
1140 representation of semantic knowledge in the human brain. *Nat Rev Neurosci* **8**, 976-987 (2007).
1141 83. Simmons, W.K. & Martin, A. The anterior temporal lobes and the functional architecture of
1142 semantic memory. *J Int Neuropsychol Soc* **15**, 645-649 (2009).
1143 84. Abel, T.J*., et al.* Direct physiologic evidence of a heteromodal convergence region for proper
1144 naming in human left anterior temporal lobe. *J Neurosci* **35**, 1513-1520 (2015).
1145 85. Scott, S.K., Blank, C.C., Rosen, S. & Wise, R.J. Identification of a pathway for intelligible speech in
1146 the left temporal lobe. *Brain* **123 Pt 12**, 2400-2406 (2000).
1147 86. Spitsyna, G., Warren, J.E., Scott, S.K., Turkheimer, F.E. & Wise, R.J. Converging language streams
1148 in the human temporal lobe. *J Neurosci* **26**, 7328-7336 (2006).
1149 87. Gorno-Tempini, M.L*., et al.* Cognition and anatomy in three variants of primary progressive
1150 aphasia. *Ann Neurol* **55**, 335-346 (2004).
1151 88. Hein, G. & Knight, R.T. Superior temporal sulcus--It's my area: or is it? *J Cogn Neurosci* **20**, 2125-
1152 2136 (2008).
1153 89. Makris, N*., et al.* Delineation of the middle longitudinal fascicle in humans: a quantitative, in
1154 vivo, DT-MRI study. *Cereb Cortex* **19**, 777-785 (2009).
1155 90. Binney, R.J., Parker, G.J. & Lambon Ralph, M.A. Convergent connectivity and graded
1156 specialization in the rostral human temporal lobe as revealed by diffusion-weighted imaging
1157 probabilistic tractography. *J Cogn Neurosci* **24**, 1998-2014 (2012).
1158 91. de Heer, W.A., Huth, A.G., Griffiths, T.L., Gallant, J.L. & Theunissen, F.E. The Hierarchical Cortical
1159 Organization of Human Speech Processing. *J Neurosci* **37**, 6539-6557 (2017).

92. Binder, J.R.*, et al.* Human temporal lobe activation by speech and nonspeech sounds. *Cereb Cortex* **10**, 512-528 (2000).
93. Cogan, G.B.*, et al.* Sensory-motor transformations for speech occur bilaterally. *Nature* **507**, 94-98 (2014).
94. Sherman, S.M. & Guillery, R.W. Distinct functions for direct and transthalamic corticocortical connections. *J Neurophysiol* **106**, 1068-1077 (2011).
95. Hu, B. Functional organization of lemniscal and nonlemniscal auditory thalamus. *Exp Br Res* **153**, 543-549 (2003).
96. Biswal, B.B.*, et al.* Toward discovery science of human brain function. *Proc Natl Acad Sci U S A* **107**, 4734-4739 (2010).
97. Seitzman, B.A., Snyder, A.Z., Leuthardt, E.C. & Shimony, J.S. The State of Resting State Networks. *Top Magn Reson Imaging* **28**, 189-196 (2019).
98. Jenkinson, M., Bannister, P., Brady, M. & Smith, S. Improved optimization for the robust and accurate linear registration and motion correction of brain images. *Neuroimage* **17**, 825-841 (2002).
99. Rohr, K.*, et al.* Landmark-based elastic registration using approximating thin-plate splines. *IEEE Trans Med Imaging* **20**, 526-534 (2001).
100. Destrieux, C., Fischl, B., Dale, A. & Halgren, E. Automatic parcellation of human cortical gyri and sulci using standard anatomical nomenclature. *Neuroimage* **53**, 1-15 (2010).
101. Destrieux, C.*, et al.* A practical guide for the identification of major sulcogyral structures of the human cortex. *Brain Struct Funct* **222**, 2001-2015 (2017).
102. Brugge, J.F.*, et al.* Coding of repetitive transients by auditory cortex on Heschl's gyrus. *J Neurophysiol* **102**, 2358-2374 (2009).
103. Nourski, K.V., Steinschneider, M. & Rhone, A.E. Electrocorticographic Activation within Human Auditory Cortex during Dialog-Based Language and Cognitive Testing. *Front Hum Neurosci* **10**, 202 (2016).
104. Power, J.D., Barnes, K.A., Snyder, A.Z., Schlaggar, B.L. & Petersen, S.E. Spurious but systematic correlations in functional connectivity MRI networks arise from subject motion. *Neuroimage* **59**, 2142-2154 (2012).
105. Vinck, M., Oostenveld, R., van Wingerden, M., Battaglia, F. & Pennartz, C.M. An improved index of phase-synchronization for electrophysiological data in the presence of volume-conduction, noise and sample-size bias. *Neuroimage* **55**, 1548-1565 (2011).
106. Kovach, C.K. & Gander, P.E. The demodulated band transform. *J Neurosci Methods* **261**, 135-154 (2016).
107. Banks, M.I.*, et al.* Cortical functional connectivity indexes arousal state during sleep and anesthesia. *Neuroimage* **211**, 116627 (2020).
108. Langs, G., Golland, P., Tie, Y., Rigolo, L. & Golby, A.J. Functional Geometry Alignment and Localization of Brain Areas. *Adv Neural Inf Process Syst* **1**, 1225-1233 (2010).
109. Satopaa, V., Albrecht, J., Irwin, D. & Raghavan, B. Finding a "Kneedle" in a Haystack: Detecting Knee Points in System Behavior. in *2011 31st International Conference on Distributed Computing Systems Workshops* 166-171 (2011).